NTNU – Trondheim
Norwegian University of
Science and Technology

Texturing of lead free piezoelectric ceramics

Dehlia Eide Brennhaugen

Materials Technology
Submission date: June 2013
Supervisor: Mari-Ann Einarsrud, IMTE
Co-supervisor: Tor Grande, IMTE
Astri Bjørnetun Haugen, IMTE

Norwegian University of Science and Technology
Department of Materials Science and Engineering

Declaration

I hereby declare that the work presented in this document has been performed independently and in accordance with the rules and regulations of the Norwegian University of Science and Technology (NTNU).

Trondheim, 21 June 2013

Dehlia Eide Brennhaugen

Preface

The following thesis documents work done for the degree of Master of Science at the Department of Materials Science and Engineering at NTNU, in the period from 25 January to 21 June 2013, under supervision of Professor Mari-Ann Einarsrud, with co-supervision from Professor Tor Grande and Ph.D. candidate Astri Bjørnetun Haugen.

I would like to thank my main supervisor Mari-Ann Einarsrud for consistent guidance and fruitful conversations. Thanks go to my co-supervisor Astri Haugen for helping me with practical aspects of my work and for always being available to discuss any issues, small or big. For always keeping the weekly group meetings at a high academic level and at the same time keeping the atmosphere light and humoristic, I would also like to thank my other co-supervisor Tor Grande, as well as the rest of the Ferroics group members.

Finally I would like to thank everyone who has helped me during this master thesis, be it by helping me with technical issues in the lab, by talking about challenging concepts, or by simply showing moral support.

Abstract

Texturing of the lead-free system $Ba_{0.92}Ca_{0.08}TiO_3$ (BCT) was investigated focusing on density, degree of texture and piezoelectric response. BCT templates were prepared in a two-step molten salt synthesis to achieve the anisotropic growth needed for the template morphology. $Ba_6Ti_{17}O_{40}$ (B6T17) templates were synthesised, and then converted to BCT through a topotactic conversion process. BCT templates with a 20-50 µm diameter range and a 2-20 aspect ratio were obtained. The templates had a Lotgering factor F_{111}=59.4%.

Textured samples were prepared by tape casting and templated grain growth. As a reference, non-textured samples were prepared, and analysed together with the textured samples. A sintered BCT laminate, with a density of 93.4%, reached a texture degree of 42.7%. The highest measured direct and converse piezoelectric coefficients were d_{33}=49±3 pCN^{-1} and d_{33}= 140 pmV^{-1} respectively. Textured materials showed an increase in piezoelectric response compared to the non-textured materials. As many samples had a weak ferroelectric response, the foundation for comparing the effects of texture was somewhat impaired. This was probably caused by a combination of the low density and impurities in the samples. However, promising results with regard to enhancing piezoelectric response by texturing was observed and should be further investigated, focusing on achieving higher densities and thus higher degrees of texture in the ceramic.

Sammendrag

Det blyfrie, piezoelektriske keramet $Ba_{0.92}Ca_{0.08}TiO_3$ (BCT) har blitt teksturert i (111) planet, og piezoelektrisk karakterisert. For å oppnå partikler med en ønsket platemorfologi har BCT templater blitt fremstilt gjennom en topotaktisk saltsmelteprosess. Forløperpartikler av typen $Ba_6Ti_{17}O_{40}$ (B6T17), som fremmer anisotrop vekst, ble brukt som utgangsstoff for den topotaktiske konverteringen til BCT. Templater med en størrelse på 20-50 µm og et størrelsesforhold (areal/tykkelse) på 2-20 ble fremstilt. BCT-templatene oppnådde en Lotgering faktor F_{111} på 59.4%.

Teksturerte keramer ble fremstilt ved båndstøping og templatfremmet kornvekst. Uteksturerte keramer med samme støkiometri ble fremstilt som referansepunkt. Høyeste tetthet og tekstur oppnådd for sintret keram var henholdsvis 93.4% og 42.7%. Den samme prøven hadde også de høyeste målte direkte og konverse piezoelektriske koeffisientene på henholdsvis 49 ± 3 pCN^{-1} og 140 pmV^{-1}. Teksturerte prøver viste seg, som ventet, å ha større piezoelektriske koeffisienter enn uteksturerte prøver. På grunn av forurensninger fra matrikspulveret som ble brukt i fremstillingen av prøvene, opplevde noen av prøvene lekkasjestrøm under testing. Dette førte til at svært få prøver kunne sammenlignes med tanke på piezoelektriske egenskaper. Fra prøvene som ble testet ser det likevel ut til at det (111) teksturerte BCT systemet kan ha lovende verdier for piezoelektrisitet, noe som berettiger videre forskning. Spesiell oppmerksomhet bør i fremtidige arbeid bli gitt til økning av tetthet og dermed også tekstur i sintrede keramer.

Contents

Declaration i

Preface ii

Abstract iii

Sammendrag iv

1. Background 1

1.1 Motivation 1

1.2 Aim of this work 2

2. Introduction 3

2.1 $BaTiO_3$ crystal structure 3

2.2 Structural requirements for ferroelectricity 3

2.3 Poling 5

2.4 Texturing 6

2.5 Topotaxy and anisotropic growth 7

2.6 Tape casting 9

2.7 Piezoelectric effects 10

2.8 Ca-doping 12

2.9 Piezoelectric characterisation 13

3. Experimental 15

3.1 BCT template synthesis 15

3.2 From powder to dense textured ceramics 16

3.3 Characterisation methods 17

3.3.1 X-ray diffraction 17

3.3.2 Lotgering factor calculations 18

3.3.3 Scanning electron microscope 18

3.3.4 Density calculations 18

3.3.5 Piezoelectric characterisation 18

4. Results 20

4.1 Template characterisation 20

4.2 Tape characterisation 25

4.3 Characterisation of sintered laminates and pellets 27

4.4 Piezoelectric characterisation 32

5. Discussion 37
5.1 Template morphology 37
5.2 Template orientation and purity 37
5.3 Tape casting 38
5.4 Density and texture of samples 39
5.5 Piezoelectric characterisation 40
6. Concluding remarks and further work 43
References 44
Appendix A - Dilatometer curve of BCT 47

1. Background

1.1 Motivation

Piezoelectricity was discovered by the Curie brothers Jacques and Pierre in 1880 [1]. Piezoelectric ceramics have since been developed over decades of research into materials which today can be used in a variety of applications like actuators, sensors and transducers to name a few [2].

The discovery of piezoelectricity led to an investigation of different polycrystalline materials, amongst them $BaTiO_3$, which was discovered to possess piezoelectric properties in the 1940's independently in different parts of the world [1]. In 1954 a new piezoelectric system was discovered which had a huge impact on the possibilities for piezoelectric applications: lead zirconate titanate (PZT). This new system was discovered to have extremely strong and temperature stable piezoelectric effects, making PZT highly suitable for a range of applications. This high degree of stability is caused by the presence of an almost vertical morphotropic phase boundary, a region in the phase diagram where piezoelectric responses are heightened and stable. Thus PZT effectively replaced weaker piezoelectric systems and dominated the market for decades to present time.

In 2003 the European Union issued a new directive stating that "Member States shall ensure that (…) new electrical and electronic equipment put on the market does not contain lead, (…)" [3]. However, an exemption from the new directive was made for "lead in electronic ceramic parts (e.g. piezoelectronic devices)" until a suitable replacement is discovered [3]. This has triggered a massive search for lead free piezoelectrics, see Figure 1.1 [2].

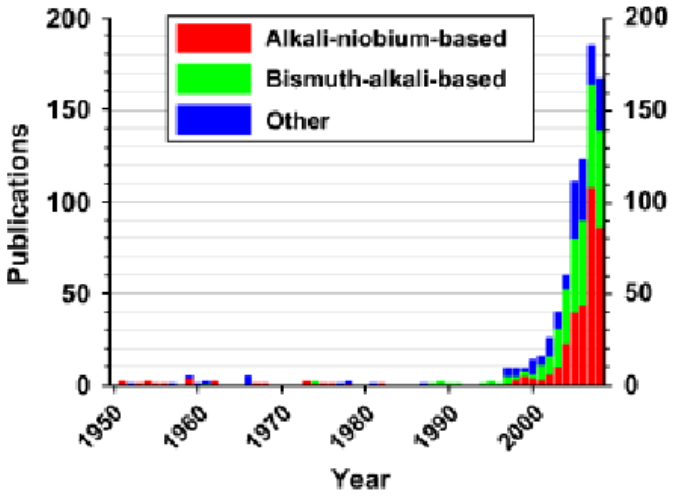

Figure 1.1: Publications on lead-free piezoceramics from 1950 to November 2008 [2].

An article published in 2009 [4] reported extremely high piezoelectric values for the system $BaCaZrTiO_3$ (BCZT), which of course led to an increased interest in this system. The BCZT system also has a morphotropic phase boundary which causes these high piezoelectric values. However, the boundary is not as stable with respect to temperature as in PZT, making the BCZT system less suitable for applications with wide temperature ranges. Different approaches to improving and stabilising the BCZT system involves focusing on promising chemical dopants, electronic structures, crystal structures, phase diagrams [2] and texturing [5].

1.2 Aim of this work

The aim of the present work is to prepare textured $Ba_{0.92}Ca_{0.08}TiO_3$ (BCT) ceramics with a preferred (111) grain orientation. The objective is to produce dense piezoelectric ceramics which can contribute to a better understanding of texturing and its effects on the piezoelectric coefficient of the BCT system by optimizing template aspect ratios, tape casting- and sintering parameters. To assist an increased understanding of the effect of texturing, the materials will be characterised, focusing on microstructure, density, chemical composition, and piezoelectric effects. The textured materials will also be compared to non-textured materials of the same chemical composition.

2. Introduction

2.1 $BaTiO_3$ crystal structure

$BaTiO_3$ (BT) is a ferroelectric and has a tetragonal perovskite structure at room temperature [6]. This means that compared to a cubic perovskite, the unit cell is slightly distorted along the c-axis as shown in Figure 2.1. Because of the Ti^{4+} ions size being slightly too small for a perfect match with the cubic perovskite structure, the Ti^{4+} displaces about 6 % to one of the corner oxygen atoms [6]. This Ti^{4+} movement results in a large dipole moment or polarisation in the tetragonal perovskite structure. Because BT is a ferroelectric, this polarisation is reversible and can be switched by applying an electric field to the crystal.

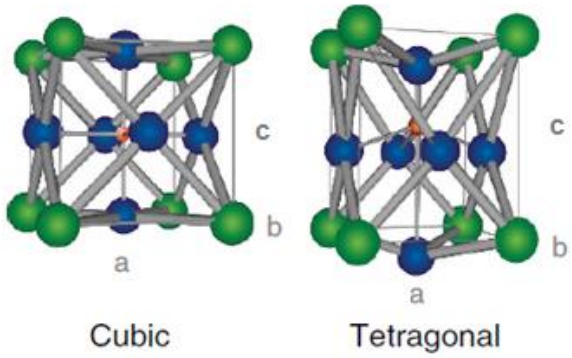

Figure 2.1: Cubic and tetragonal perovskite. Red: Ti^{4+}, blue: Ba^{2+}, green: O^{2-} [7].

2.2 Structural requirements for ferroelectricity

There is a two-way relationship between polarisation and mechanical stress in piezoelectrics, giving rise to two opposing effects: the direct effect (generator, mechanical stress produces electrical charge), and the converse effect (motor, electrical field produces mechanical movement)[8]. Piezoelectricity is a material property which depends partly on crystal symmetry. Figure 2.2 below shows a schematic of the symmetry requirements for piezo- and ferroelectrics.

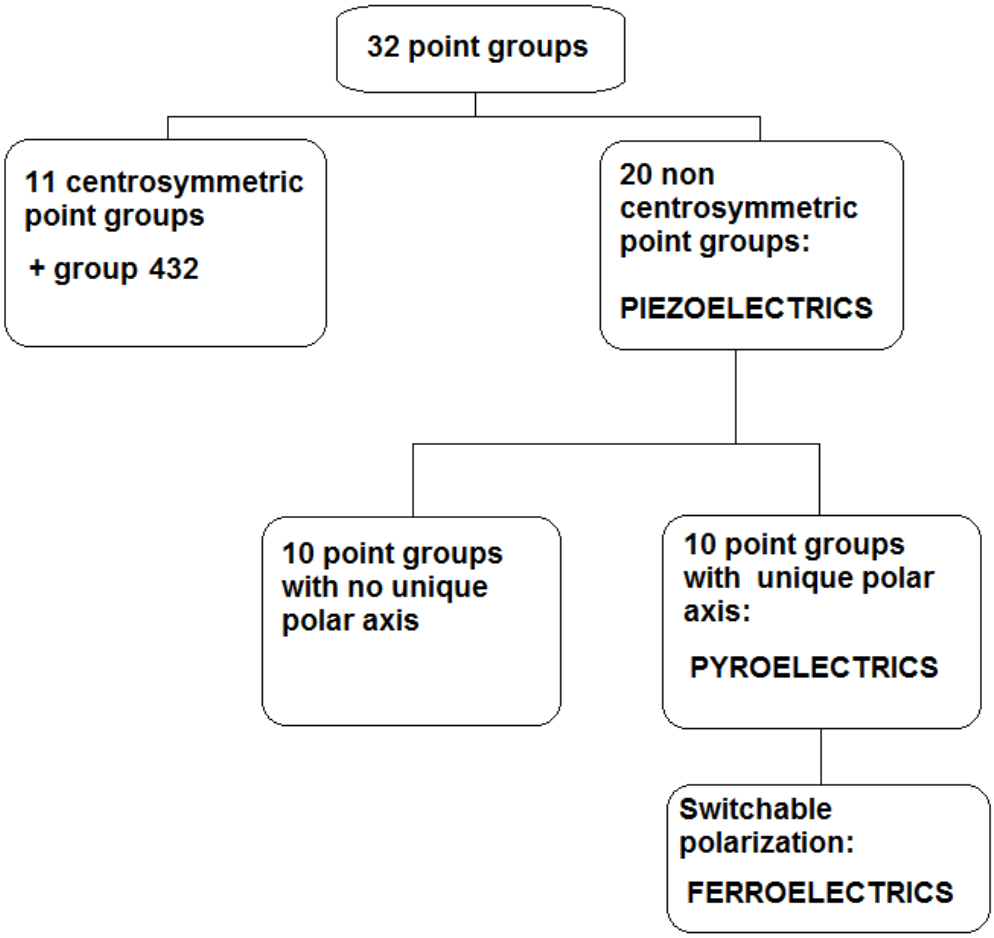

Figure 2.2: Schematic overview over crystallographic symmetry requirements for ferroelectrics.

As visible from Figure 2.2 ferroelectrics is a subgroup of piezoelectric materials meaning that all ferroelectrics are also piezoelectric but not vice versa. The requirements for having a ferroelectric material are to have a non centrosymmetric point group and a unique polar axis where polarisation can be switched by applying an external electric field. BT has a tetragonal perovskite structure at room temperature, and belongs to the space group P4mm [9] which is a non-centrosymmetric space group. This means that there is no centre of symmetry in the crystal around which all point coordinates can be inverted going from (x,y,z) to (-x.-y,-z) [10]. In the P4mm space group of the tetragonal perovskite the unique polar axis is along the [001] direction [10].

Predicting ferroelectricity purely on a theoretical structural basis is not yet possible, as the mechanisms behind ferroelectricity are not yet well understood. Various models have been proposed to predict ferroelectric behaviour, considering complex lattice vibration states, however none have yet reached a broad acceptance in the research community. As a result ferroelectricity must be determined by empirical testing in combination with a theoretical understanding of the crystal symmetry [11].

2.3 Poling

In a polycrystalline ceramic where several unit cells in a cluster have the same polarisation orientation we have what is known as a domain. Different domains in a ceramic are divided by so called domain walls where one domain orientation gradually becomes another over a width of several tens of nanometers [12]. When a material is poled, its domains are oriented in the same direction as depicted in the right hand side of Figure 2.3, where one arrow represents one domain in the material. When applying an electric field to an un-poled ferroelectric, the domains will try to align themselves so as to use the polarisation to counteract the applied field [8].

Unpoled ferroelectric piezoelectrics have a zero net polarisation value. Even though the entire material is consisting of polarised domains, all the domains have a random orientation, see Figure 2.3 a), which results in a zero net polarisation of the ceramic material. However, by applying an electric field to the ferroelectric material, most domains will align themselves to counteract the applied field and create a measurable net polarisation of the material, Figure 2.3 b). When removing the field (Figure 2.3 c)) most domains will retain their orientation resulting in a net polarisation value for the material. Because of ferroelectrics being able to retain a polarisation after removing the applied field, a characteristic hysteresis loop will occur for this material as shown in Figure 2.3. This alignment is only possible if the piezoelectric is also a ferroelectric. An applied electric field will not affect the domains of a non-ferroelectric piezoelectric as the polarisations are not switchable (Figure 2.2).

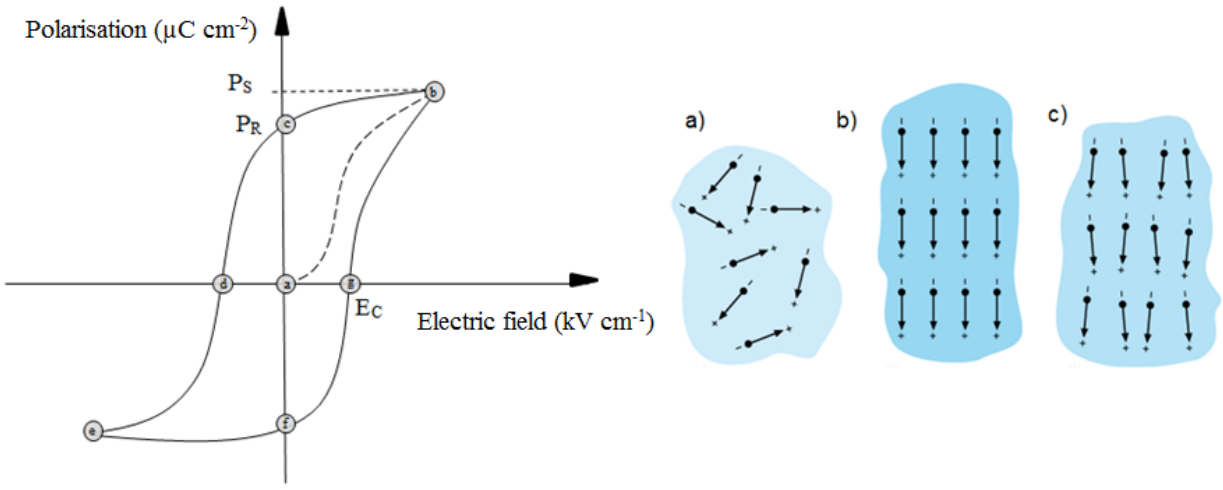

Figure 2.3: Characteristic hysteresis loop for a ferroelectric material. a) unpoled, b) P_S = saturation polarisation, c) P_R = remnant polarisation. E_C = coercive field in the left hand figure. Right hand figure adapted from reference [13].

When applying a positive electric field, the initial polarisation P_S is achieved. When the field is switched off, the polarisation drops to P_R. If a negative electric field is applied, this will result in a negative P_S value marked by "e" in Figure 2.3. These two polarisation extremities are often referred to as "polarisation up" and "polarisation down" [8] and are especially relevant in terms of thin film memory applications.

The discovery of poling has made it possible to create piezoelectric ceramics where the different domains in a crystal can be permanently aligned instead of all the domains cancelling each other out resulting in a zero net polarisation [8].

To convert the material back to its original chaotic state the material is heated above the Curie temperature where all poling effects are lost [8]. Pure $BaTiO_3$ has a relatively low Curie temperature (T_C =120 °C) explaining why this piezoelectric is mainly used in low-temperature applications like capacitors, rather than transducers which are usually operated at higher temperatures [8].

2.4 Texturing

In a non-textured material, the switching of polarisation during poling is often hindered by misoriented grains [7]. One way to increase the effects of poling is to orient the polar axis in each grain in the same direction. This can be achieved through texturing which changes the chaotic ordering of domains, into a more ordered structure where piezoelectric properties approach those of a single crystal [14]. Texturing makes it possible to better utilise the anisotropic nature of piezoelectric constants as will be described in Chapter 2.7.

The benefits of texturing have been established by numerous researchers on a variety of piezoelectric systems [15]. An increase in texture by 27% and a direct d_{33} = 270 pCN^{-1} was reported by Ohara *et al.* [16] for the $BaTiO_3$ system. This d_{33} value is increased 1.7 times compared to non-textured BT.

There are several texturing techniques, one of which is known as templated grain growth (TGG) where anisotropic particles and equiaxed particles are mixed to obtain a high density ceramic upon sintering. When the template and matrix particles have the same composition, the growth during sintering is called homoepitaxial templated grain growth [15]. The mixture of anisotropic particles (hereafter referred to as template particles) and equiaxed particles (hereafter referred to as matrix particles) will result in a textured material as a result of two possible mechanisms. The first mechanism involves template particles growing on the expense of matrix particles, thus determining the dominating orientation of the material. This is often referred to as Ostwald ripening, where larger particles grow at the expense of smaller particles to minimise the surface boundary energy. The second mechanism involves matrix particles adopting the texture of template particles at matrix-template interfaces [14]. The degree of texture achieved is highly dependent upon the density of the material as pores act as barriers for template grain growth [15]. When density exceeds 95% the templates are initially able to grow rapidly. Eventually the growth rate slows down as templates become large and start to impinge one another. Reaching this rapid growth state substantially increases density which has shown to be of paramount importance to achieve highly textured materials.

2.5 Topotaxy and anisotropic growth

Obtaining perovskite structured templates with a high aspect ratio in one-step procedures has proved to be challenging because of the structure's lack of anisotropic growth [17]. This is why topotactic conversion synthesis routes have been developed, making high aspect ratios achievable through the use of precursor templates which control both orientation and morphology of the resulting templates. A topotactic reaction is a solid state reaction where the atomic structure and morphology of the crystal is preserved to a large degree, only allowing small dimensional changes in one or more directions [18]. A topotactic synthesis route involves choosing a suitable precursor material with the desired morphology and topotactic relationship to the end product. This precursor will then to some extent control the morphology during the conversion process from precursor to final product.

To obtain $Ba_{0.92}Ca_{0.08}TiO_3$ (BCT) templates with a (111) orientation, the precursor $Ba_6Ti_{17}O_{40}$ (B6T17) was chosen because of its topotactic relationship to the end product [14, 19, 20]. BCT and B6T17 are related through the orientation relationship given by Equation 2.1 [21].

$$(001)_{B6T17} \;||\; (111)_{BCT} \tag{2.1}$$

Because of the layered structure of the B6T17 [21] this system has an anisotropic surface energy making growth in one specific direction preferable to the others. This results in B6T17 having a plate-like morphology. Figure 2.4 depicts a suggested growth mechanism where a precursor with a layered structure partially exfoliates during its conversion to the templated perovskite [17]. Depending on orientation of the crystallites in this process, the end result will either be a single crystal or a highly oriented polycrystal consisting of multiple crystallites. Controlling the temperature and holding time during template conversion is key to optimise the template size and aspect ratio [14]. The salt species used for the flux in the molten salt synthesis can also influence template morphology.

Even though a topotactic relationship has been reported by several different sources, other mechanisms which could cause the conversion should be mentioned. One alternative mechanism is the solid solution and precipitation mechanism where the BCT nucleates heterogeneously on the B6T17 surface and grows epitactically on the surface of the precursor templates.

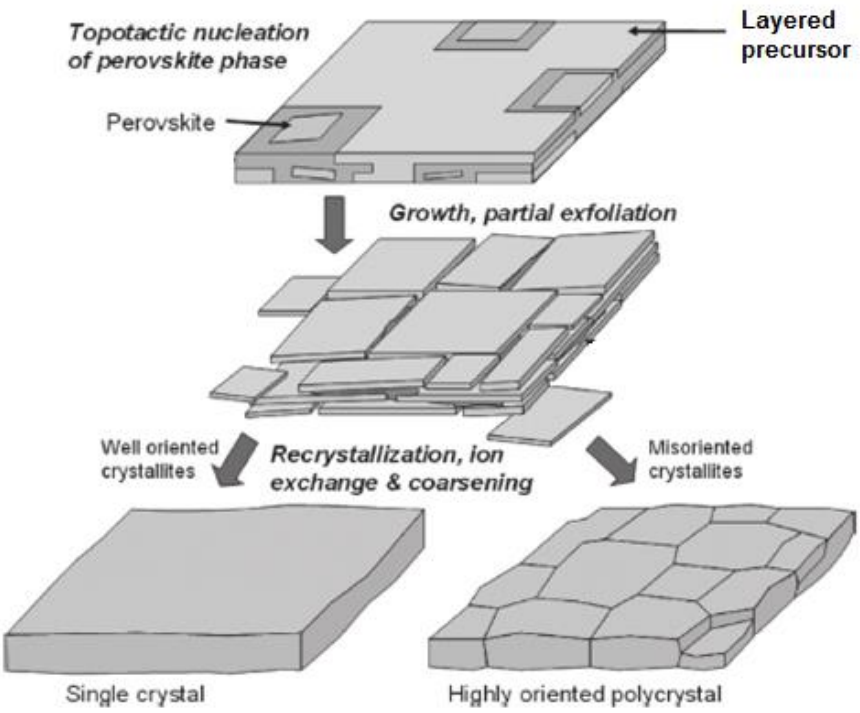

Figure 2.4: Growth and conversion mechanism of layered structure to perovskite structure through a topotactic conversion. Adapted from reference [17].

There have been reported several successful attempts at synthesising (111) oriented BT templates, using (001) oriented B6T17 templates as precursor in a topotactic conversion process [5, 20, 22]. When synthesising $Ba_6Ti_{17}O_{40}$ (B6T17) from $BaTiO_3$ and TiO_2, there are many possible stoichiometries close to the Ba:Ti 6:17 ratio of B6T17. This is illustrated by the section of the BaO-TiO_2 system phase diagram in Figure 2.5, [23]. The two neighbouring stoichiometries are $BaTi_2O_5$ and $Ba_4Ti_{13}O_{30}$ which have higher and lower Ba:Ti ratios, respectively. This is why extra care must be taken when preparing the precursor templates, so that the stoichiometry achieved is close to the stoichiometry with the desired topotactic relationship to the end product. If the reaction does not reach the desired Ba:Ti ratio, this could affect the crystal structure of the phase and eventually affect the conversion process and the degree of orientation obtainable in the BCT.

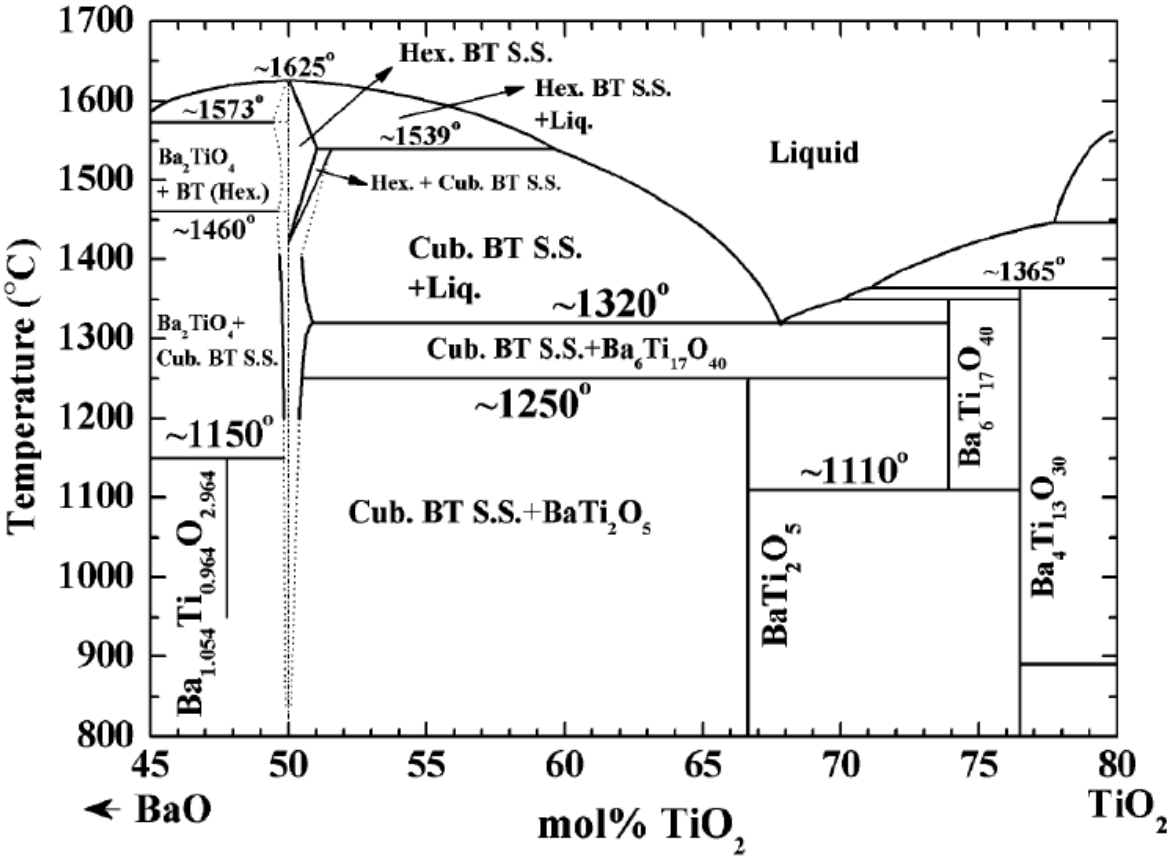

Figure 2.5: Pseudo-binary phase diagram of the BaO-TiO_2 system [23].

2.6 Tape casting

When using TGG it is important to align the templates in the matrix powder before heating the sample to sintering temperatures. Tape casting is an excellent way of aligning templates, and maximise the degree texture. Figure 2.6 depicts a schematic of how templates in a slurry are aligned during tape casting [24].

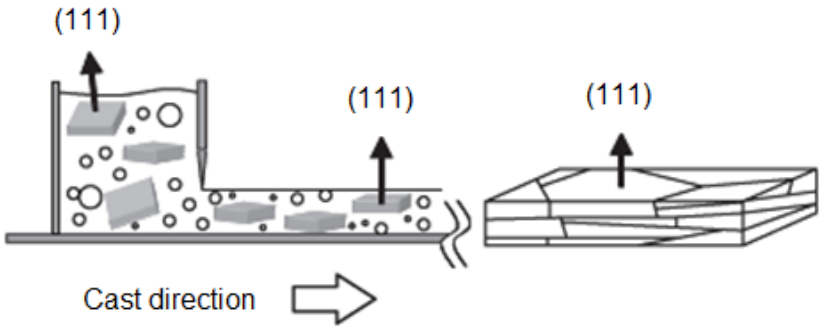

Figure 2.6: Schematic of tape casting a slurry containing a mixture of matrix and template particles. The laminate on the right shows the texture orientation of the final laminated and sintered ceramic. Adapted from reference [24].

There are several tape casting factors which influence the degree of texture achieved. According to Kim *et al.* [25] there are two types of forces which influence slurry behaviour during casting, namely pressure driven forces and viscous driven forces. The ratio between these two is given the parameter name Π, and is described by Equation 2.3,

$$\Pi = \frac{\Delta P H^2}{2\mu L U} \tag{2.3}$$

where ΔPH^2 are the pressure driven forces and 2μLU are the viscous driven forces. Here ΔP is the pressure exerted by the slurry, H is the doctor blade gap, μ is the viscosity, L is the width of the doctor blade, and U is the casting velocity [25]. The viscous forces are the ones responsible for shear forces and the rotation and alignment of templates in the slurry. The degree of orientation is therefore a function of casting velocity, slurry viscosity and template concentration in the slurry.

2.7 Piezoelectric effects

Piezoelectricity can be quantified by the piezoelectric coefficient, d_{ij}, which indicates the amount of charge generated per unit of applied stress for the direct effect, and the amount of strain produced by an applied field for the converse effect.

Depending on the direction of the applied field and the direction of the polarisation measurements, different types of d_{ij} values can be measured. These different piezoelectric coefficients are distinguished from one another by using subscripts. Figure 2.7 illustrates the many possible combinations of longitudinal, transverse and shear effects. For example the coefficient d_{33} indicates that the polarisation is occurring longitudinal to the applied stress, while the coefficient d_{31} indicates a transverse piezoelectric response. The curved arrows in Figure 2.7 indicate shear responses to the applied field. An example of a shear piezoelectric coefficient is the d_{15} coefficient.

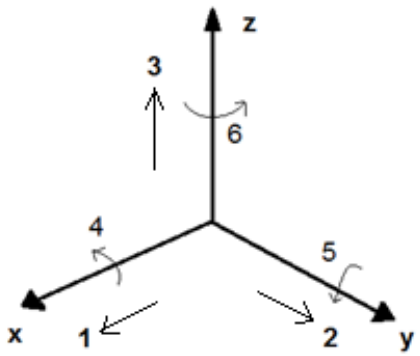

Figure 2.7: Schematic of directions and indexing of d_{ij} subscripts. 1, 2 and 3 denote tensile components along x, y and z axes, while 4, 5 and 6 denote shear components about the x, y and z axes respectively.

The different piezoelectric effects are competing when measuring the total piezoelectric response of a specific material [26]. This leads to classifying piezoelectrics as either being

"extenders" (longitudinal response like d_{33} dominates) or "rotators" (shear response like d_{15} dominates). Equation 2.4 [26] gives the combined effects of transverse, shear and longitudinal contributions on the longitudinal piezoelectric coefficient d_{33}*, as a function of θ which is the angle away from the polarisation direction in the material.

$$d_{33}^{*} = (\cos\theta \sin^2\theta)d_{31} + (\cos\theta \sin^2\theta)d_{15} + \cos^3\theta d_{33} \qquad (2.4)$$

In a ceramic, all these effects contribute to the measured response d_{33}*. It is therefore relevant to decompose the different contributions to the piezoelectric coefficient, so as to identify the optimal texture orientation for maximised piezoelectric responses. At room temperature $BaTiO_3$ is a rotator type of piezoelectric, because the d_{15} is much larger than d_{33}, see Figure 2.8 a) [27]. This means that at room temperature (300 K) $BaTiO_3$ has its highest longitudinal piezoelectric response when measuring at an angle away from the polar axis [001], with a peak around θ=55°, see Figure 2.8 b) [27]. This is also confirmed by Equation 2.4, because at a certain angle the contribution from the shear coefficient d_{15} is maximised.

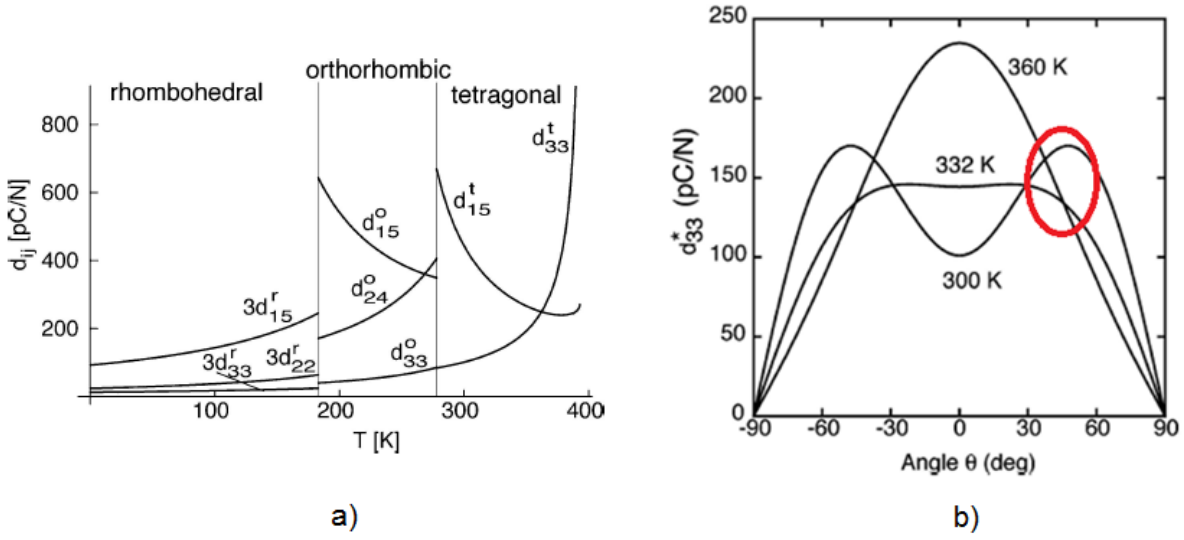

Figure 2.8: shows a) the domination of the shear coefficient d_{15} for $BaTiO_3$, thus making it a rotator at room temperature [27], and b) d_{33}* as a function of angle away from the polarisation direction [27]. The red circle in b) locates the lowest variation in response when changing the temperature.

From Figure 2.8 it is evident that as the temperature is increased, $BaTiO_3$ changes its response from being a rotator to being an extender. This is assumed to be caused by the proximity to a phase transition between the tetragonal and orthorhombic phases of $BaTiO_3$ [26].

From Figure 2.8 b) the least amount of change in d_{33}* when increasing the temperature is found at an angle of about 55° away from the polarisation axis, meaning that at this specific angle the measured piezoelectric response is most stable with respect to temperature change, see red circle. The direction in the tetragonal unit cell closest to this peak value is found between the polarisation axis [001] and the [111] direction, with an angle θ=54.7° separating the two, see Figure 2.9. By texturing in the (111) plane the piezoelectric effects are stabilised

as a function of temperature, making this specific orientation interesting for piezoelectric investigations.

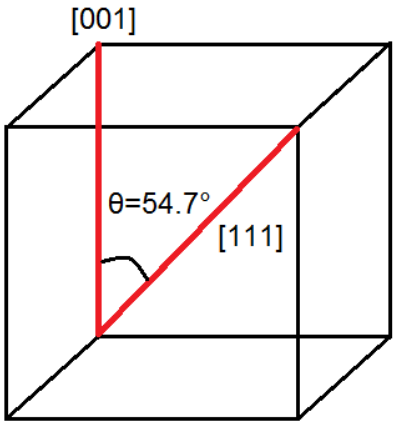

Figure 2.9: The angle between the polarisation axis [001] in BCT and the [111] direction.

2.8 Ca-doping

When doping $BaTiO_3$ with $CaTiO_3$, the Ca^{2+} goes into the A-site of the ABO_3 perovskite structure, if prepared by a salt flux method [9]. This stabilises the tetragonal phase to lower temperatures, as can be seen in Figure 2.10. The Ca^{2+} also increases the Curie temperature slightly (tetragonal to cubic transition), showing a peak value at 8 mol% Ca [28]. This phase stabilisation is why the $Ba_{0.92}Ca_{0.08}TiO_3$ (BCT) stoichiometry is interesting to investigate further.

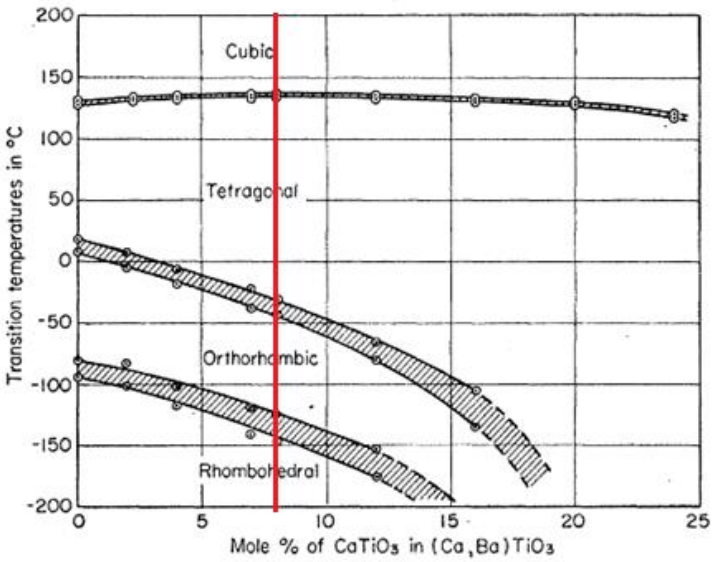

Figure 2.10: Phase transition temperatures of $Ba_{1-x}Ca_xTiO_3$ as a function of molar ratio of added $CaTiO_3$ [28]. The red line indicates 8 mol% Ca.

2.9 Piezoelectric characterisation

By using piezoelectric measurement equipment several characteristic traits of a ferroelectric material can be investigated. A relevant property of the textured BCT is the measured d^*_{33} value (hereafter simply denoted d_{33}), usually measured after poling the material. For this specific stoichiometry ($Ba_{0.92}Ca_{0.08}TiO_3$) measured d_{33} values from 149-190 pCN^{-1} have been reported [1, 29]. It should be noted that these values were measured from non-textured BCT. Textured BT has been reported to have a d_{33} = 270 pCN^{-1} [16].

As shown in Figure 2.3 polarisation of the material as a function of the applied field strength reveals values like coercive field, saturation polarisation and remnant polarisation. By plotting displacement, or strain, as a function of the applied, bipolar electric field, a so called butterfly loop will appear for a piezoelectric material, as shown in Figure 2.11 a). By plotting strain versus a unipolar applied electric field, the d_{33} can be calculated from the average slope of this curve, as can be seen in Figure 2.11 b). For specific applications a large strain response in the material is desirable, e.g. actuators where the converse piezoelectric effect is used, an increase in strain response means an increased effect.

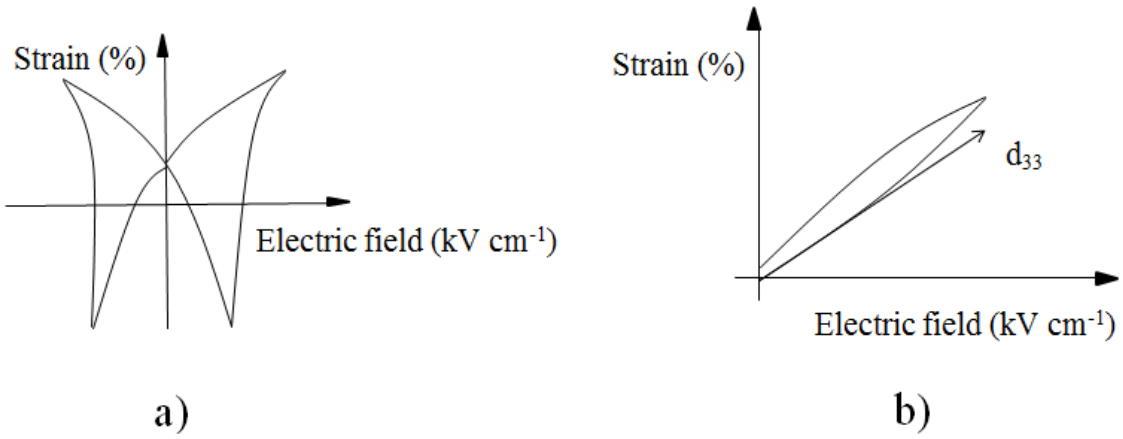

Figure 2.11: a) Butterfly loop showing strain versus bipolar electric field for a piezoelectric material and b) strain versus unipolar field where d_{33} is calculated from the slope of the curve as indicated.

Figure 2.12 shows characteristic current versus field behaviour for a ferroelectric ceramic. As the applied field reaches the coercive field strength, the polarisation in the ferroelectric is shifted, and an instantaneous current peak is registered. After the polarisation has shifted, the current response drops back to zero. When an applied reverse field reaches the negative coercive field the polarisation switches back to its original direction. Compared to a single crystal the coercive field of a ceramic is much higher. In a ceramic, neighbouring grains constrain each other's orientation making a higher field required to shift the direction of polarisation, than in a single crystal where there are no neighbouring grains. A normal coercive field for single crystal BT is around 1 $kVcm^{-1}$ [1] and for polycrystalline BT it is around 5.5 $kVcm^{-1}$ for a textured material [15].

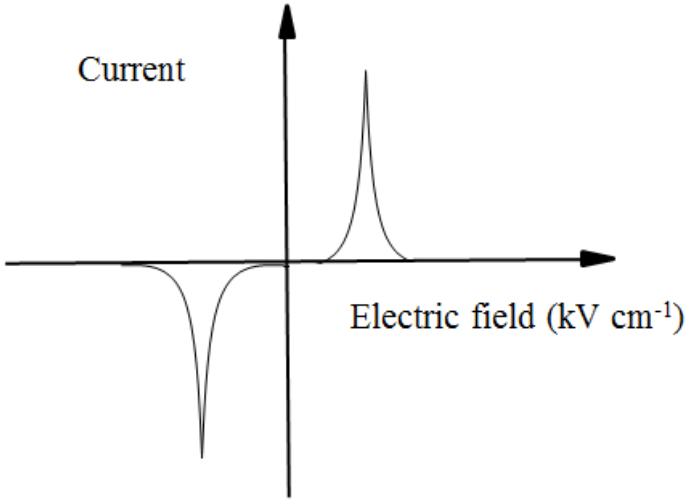

Figure 2.12: Current versus electric field for a typical ferroelectric material. The peaks indicate a switching of the polarisation direction.

3. Experimental

3.1 BCT template synthesis

The (111) oriented BCT templates were prepared by a molten salt synthesis as described by Lv *et al.* [22]. Reactants are listed in Table 3.1, including degree of purity and supplier.

Table 3.1: List of reactants used in BCT synthesis.

Reactant	Purity (%)	Supplier
$BaTiO_3$ (BT)	99.0	Sigma-Aldrich
TiO_2 (Anatase)	99.8	Sigma-Aldrich
NaCl	≥99.5	Sigma-Aldrich
$CaCO_3$	99.95-100.05	Sigma-Aldrich
$BaCO_3$	≥99.0	Sigma-Aldrich

$Ba_6Ti_{17}O_{40}$ (B6T17) particles were prepared by mixing $BaTiO_3$ (2 g) and TiO_2 (1 g) powder in a molar ratio of 6:9. The excess Ba^{2+}, was introduced to avoid the formation of $Ba_4Ti_{13}O_{30}$ [22]. BT and TiO_2 were mixed dry in a mortar for about 10 min. NaCl (3 g) was added to the mixture in a weight ratio of 1:1 and mixed for another 10 min. The homogenised mixture was then placed in an alsint crucible with a lid and heated in a Naberterm L3/12 P330 furnace to 800 °C for 1 hour to melt the NaCl and then 1150 °C for 3 hours to complete the reaction in the salt flux given by Equation 3.1. Heating and cooling rates were 200°C/hour.

$$6BaTiO_3 + 11TiO_2 \rightarrow Ba_6Ti_{17}O_{40} \quad (3.1)$$

After the heat treatment, the resulting B6T17 was separated from the flux by filtering and washing with hot distilled water (3 l), and dried at 80°C for a minimum of 2 hours. Complete washing was checked by adding $AgNO_3$ to the filtered water to check for visible AgCl precipitation.

The obtained B6T17 templates were then converted to $Ba_{0.92}Ca_{0.08}TiO_3$ (BCT) templates in a molten salt conversion process by adding $CaCO_3$, $BaCO_3$ and NaCl. The water content of $CaCO_3$ and $BaCO_3$ was investigated and found to be 0.06 and 0.11 wt% respectively. Because of the low water content, reactants were not dried prior to use. The molar ratio between BCT and $CaCO_3$ and $BaCO_3$ was 1:9.7:1.3 in order to achieve a doping of 8mol% Ca on the perovskite A-site. The reaction is described by Equation 3.2.

$$Ba_6Ti_{17}O_{40} + 1.3CaCO_3 + 9.7BaCO_3 \rightarrow 17Ba_{0.92}Ca_{0.08}TiO_3 + 11CO_2\,(g) \quad (3.2)$$

First a mixture of $CaCO_3$ (0.16 g) and $BaCO_3$ (2.25 g) was mixed in a mortar for 5 min. NaCl (5 g) was then added in a weight ratio of 1:1 with the total weight of reactants and mixed for 5-10 min. The B6T17 templates (2.7 g) were added and mixed for 3 min. Reactants were placed in an alsint crucible with a lid. The molten salt conversion took place in a Naberterm L3/12 P330 furnace at 1170 °C for 5 hours with heating and cooling rates of 200°C/hour. The BCT templates were separated from the NaCl by filtering and washing with hot distilled water (3 l) with AgCl testing as described above, and dried at 80°C for a minimum of 2 hours.

3.2 From powder to dense textured ceramics

A flow chart showing the procedure from powder to dense, textured ceramics is shown in Figure 3.1. The slurry for tape casting was prepared by mixing the constituents listed in Table 3.2. The dry content in the three first tapes consisted of 10 wt% templates and 90 wt% matrix powder, while the fourth tape consisted of 20 wt% templates and 80 wt% matrix powder. One matrix powder batch (no. 288) was used in the first two tapes, and another batch (no. 313) was used in the third and fourth tapes. The fourth tape had a higher dry content ratio than the first three tapes, making it slightly more viscous. All parameters for each tape are listed in Table 4.4 in the results chapter.

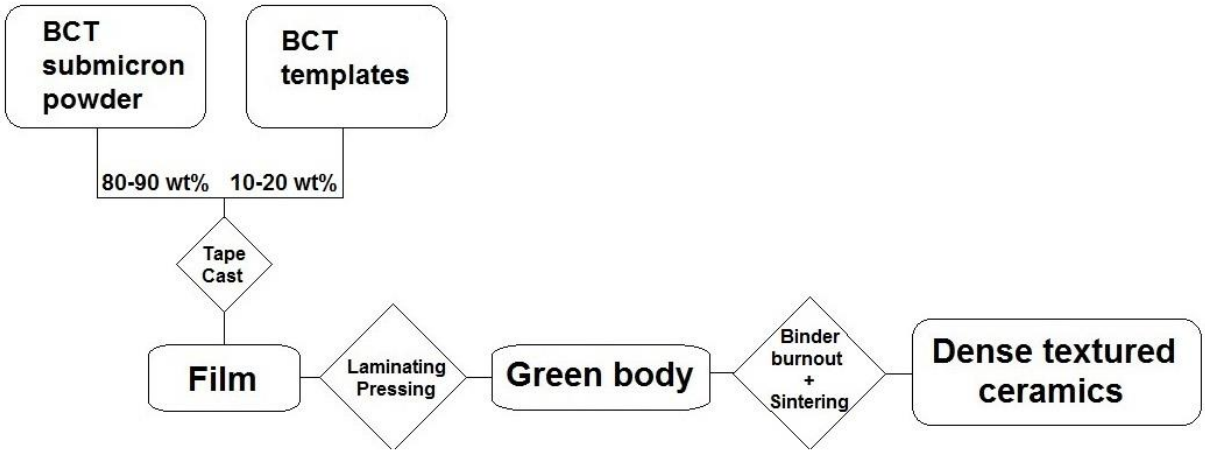

Figure 3.1: Procedure flow chart from powder to dense, textured ceramics.

Table 3.2: Weight ratios of constituents of slurry for tape casting.

Function	Chemical	Supplier	Weight (g)
Powder	BCT templates	-	1-2.40
Powder	BCT matrix powder	CerPoTech AS	9.00
Solvent	Distilled water	-	11.96
Dispersant	Darvan C-N (Ammonium polymethacrylate)	R. T. Vanderbilt Company, Inc.	0.04
Binder	Solution of 15 wt% PVA (polyvinyl alcohol) in distilled water	Merck	11.32
Plasticizer	PEG (polyethylene glycol)	Fluka	0.29
Defoamer	PPG (polypropylene glycol)	Acros Organics	0.09

First the BCT matrix powder was mixed with solvent and dispersant and ball milled at 60 rpm for 5 hours. The binder was added, along with plasticizer and ball milled for another 16-24 hours. BCT templates were added to the mixture along with 2 drops of defoamer. This was stirred for 3 hours using a magnetic stirrer at a very slow stirring rate of 100 rotations per minute. The slurry was deaired for 30 minutes using a Branson 5510 Ultrasonic bath, evacuated at 20 mbar for 10 minutes and finally aged for 30 minutes without stirring. The prepared slurry was cast on a Mylar film using a Table Top Caster TTC-1200 with two different casting speeds: 5 cm/min and 55 cm/min and left to dry in air at room temperature for 16-20 hours. Specific casting parameters for each tape are listed in Table 4.4 in the results chapter.

The resulting tapes were cut into 1.5x1.5 or 1x1 cm squares, stacked and laminated using a hydraulic hot press (Carver, Inc.) with a temperature of 70°C for 10 minutes at a pressure of 30-45 MPa, to make a 2-3 mm thick compact. Binder and other organic compounds were burnt out in a LabStar 1200/4 furnace with a two-step heating program: first the laminate was heated to 180 °C with a heating rate of 30 °C/hour, and then to 600°C with a heating rate of 12 °C/hour. The laminate was kept at 600°C for 6 hours and then cooled to room temperature with a cooling rate of 200 °C/hour. After the binder burnout, the laminate was sintered in a Lenton UAF 15/10 furnace in air at 1300–1350°C for 14 hours. Heating and cooling rates were 200 °C/hour. The choice of sintering temperature was done by dilatometer analysis of the matrix powder BCT (batch 288), as shown in Appendix A [30].

As a non-textured reference to the textured laminates, pellets consisting only of matrix powder were prepared using a Compac Hydraulik uniaxial press. The pellets had a diameter of 1 cm. The pellets were sintered together with the laminates and then characterised in the same way as the laminates as described in the following chapter. A summary of laminate and pellet preparation parameters are given in Table 4.5 and Table 4.6 in the results chapter.

3.3 Characterisation methods

3.3.1 X-ray diffraction

The different intermediate products including B6T17 templates, BCT templates, green tapes and sintered materials were analysed by XRD using a Bruker D8 FOCUS diffractometer with a 2θ range of 20 to 50 degrees using CuKα radiation. Powder samples were prepared for XRD by two methods in order to study the effects of the (111) oriented templates. Particles which were dispersed in ethanol (100%) and spread on a silicon single crystal are hereafter denoted as cast samples. Dry particles which were spread on a silicon single crystal with a thin layer of vacuum grease for improved adhesion are hereafter denoted as dry samples.

3.3.2 Lotgering factor calculations

Degree of texturing was calculated using the relative intensities of diffractions in the x-ray diffractograms, a method known as the Lotgering method [31] which yields a relative volume of textured material called the Lotgering factor. This factor, denoted F_{111}, was calculated using Equations 3.3 to 3.5.

$$F_{111} = \frac{P - P_0}{1 - P_0} \tag{3.3}$$

$$P = \frac{\sum I_{(111)}}{\sum I_{(hkl)}} \tag{3.4}$$

$$P_0 = \frac{\sum I_{0,(111)}}{\sum I_{0,(hkl)}} \tag{3.5}$$

$I_{(111)}$ is the diffracted intensity of the enhanced plane (111), while $I_{(hkl)}$ is the diffracted intensity of all measured planes in the textured sample. $I_{0,(111)}$ and $I_{0,(hkl)}$ are intensities from a non-textured reference sample of $Ba_{0.93}Ca_{0.07}TiO_3$ (PDF: 04-006-0819).

3.3.3 Scanning electron microscope

The microstructure of templates, tapes and sintered materials were characterised using a LVSEM Hitachi S-3400N in secondary electron mode and backscattered electron mode. Both unpolished and polished surfaces of sintered ceramics were investigated as well as cross sections. Tapes were fractured by different methods like cutting with scalpel and scissors, tearing by hand and fractured while immersed in liquid nitrogen. The most brittle fracture was achieved when fracturing the tapes while immersed in liquid nitrogen. These fracture surfaces were therefore characterised. Samples were carbon-coated to avoid charging during SEM investigations.

3.3.4 Density calculations

Density of sintered samples was analysed using the Archimedes method. By weighing the samples dry (m_1), immersed in isopropanol (m_2) and soaked by isopropanol (m_3), the density was calculated using Equation 3.6 [32].

$$\rho_{sample} = \frac{m_1}{(m_3 - m_2)} \rho_{isopropanol} \tag{3.6}$$

3.3.5 Piezoelectric characterisation

Samples with a density above 90% were prepared for piezoelectric characterisation. Pellets and laminates were grinded to a thickness of about 1-2 mm. Table 3.3 gives an overview of the densities and aspect ratios for the tested samples.

Table 3.3: Density and aspect ratios of piezotested sintered laminates and pellets.

Sample	Colouring	Density (%)	Area (mm^2)	Thickness (mm)	Aspect ratio
L3	evenly brown	93.4	132.93	0.97	13.7
L4	unevenly grey	91.3	83.86	0.83	10.1
P5	unevenly brown	92.1	52.39	2.21	2.4
P6	unevenly grey	91.7	53.69	1.72	3.1

After grinding, the samples were washed in ethanol (100%), cleaned in a Branson 5510 Ultrasonic bath for 10 min and dried (80 °C for 15 min). Silver electrodes were applied using Dosilac Conductive Silver Spray. The electrodes were burnt in over night at 200°C using a Binder Vacuum Drying Furnace VD 23.

Sintered samples were characterised using an APC YE2730A d_{33}-meter and an aixPES piezo tester. The piezoelectric characterisation consisted of first applying a bipolar electric field to the samples with increasing field strength (5-20 kV/cm), and then applying a unipolar field with decreasing field strength (20-5kV/cm). Direct d_{33}-values were measured with the d_{33}-meter before and after testing. All testing was done at room temperature with a frequency of 0.25 Hz.

4. Results

4.1 Template characterisation

Figure 4.1 a)-c) depicts three batches of B6T17 templates prepared by molten salt synthesis, and d) templates obtained by Lv *et al.* [22]. The three batches of B6T17 were all prepared with the same synthesis parameters, given in Table 4.1. The calculated aspect ratios are also given in Table 4.1. The three B6T17 batches have comparable morphologies, making the results fairly repeatable, while the results from the article by Lv *et al.* report a much lower thickness as well as a narrower diameter range resulting in a higher aspect ratio.

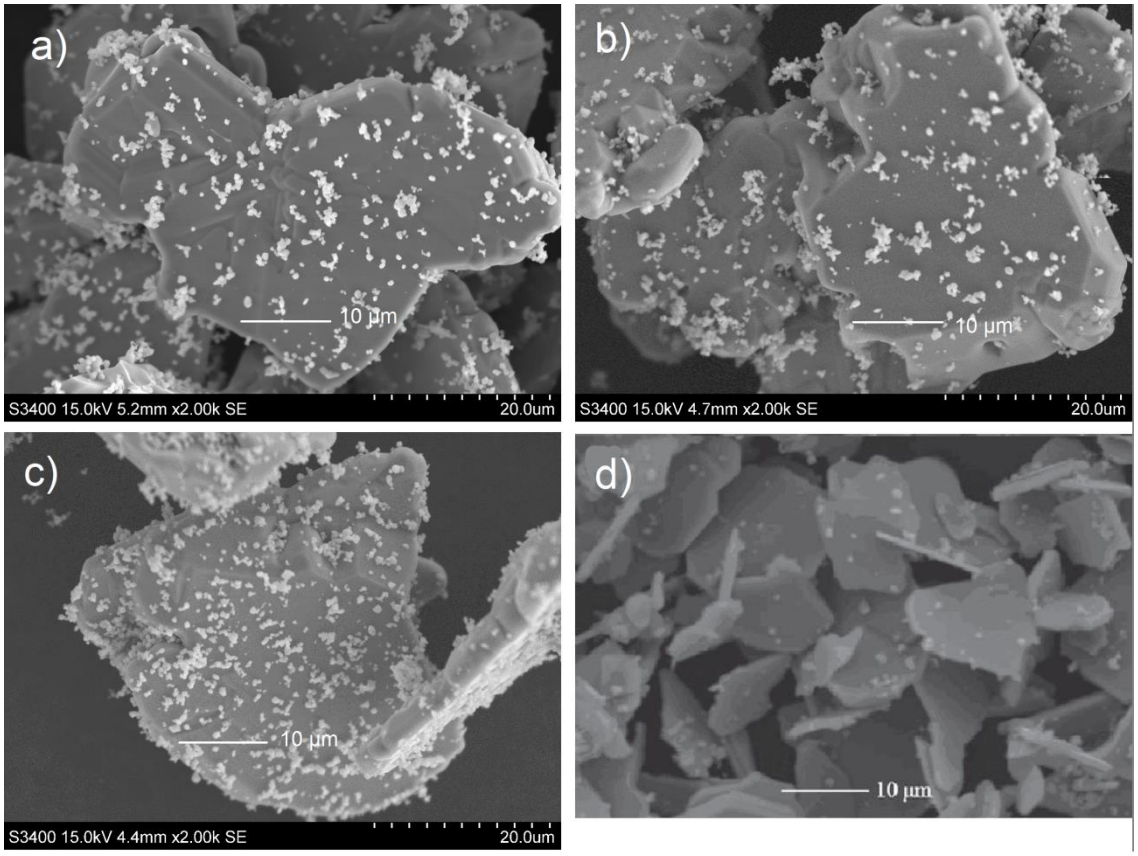

Figure 4.1: B6T17 powder batches, all prepared at 1150°C for 3 hours, a) B6T17 batch 1, b) B6T17 batch 2, c) B6T17 batch 3, d) B6T17 prepared by Lv *et al.* [22]

Table 4.1: Calculated aspect ratios for synthesised B6T17 precursor templates.

B6T17 batch number	Synthesis temperature (°C)	Synthesis time (h)	Diameter (µm)	Thickness (µm)	Aspect ratio
1	1150	3	29 – 45	3 – 7	4 – 14
2	1150	3	22 – 46	3 – 6	3 – 17
3	1150	3	24 – 54	3 – 7	3 – 20
Lv *et al.* [22]	1150	3	10 – 20	0.5 – 1	10 – 40

The first conversion from B6T17 to BCT was done at 1170°C, which resulted in a large aspect ratio compared to Lv *et al.*'s templates. In an attempt to minimise template thickness the second conversion took place at 1150°C. Lowering the temperature was, however, not effective in minimizing the template thickness and the third batch was therefore converted at the original temperature of 1170°C. Micrographs of BCT batches 1-3 in addition to a reference micrograph taken from the article by Lv *et al.* [22] can be seen in Figure 4.2 (note that the reference micrograph is of undoped BT). As can be seen in Table 4.2 the best aspect ratios were obtained at a conversion temperature of 1170°C. The BT templates obtained by Lv *et al.* are much thinner than the ones obtained in the present work. The templates obtained in the present work are larger than the ones reported by Lv *et al.* In total a wider aspect ratio range was obtained in the present work.

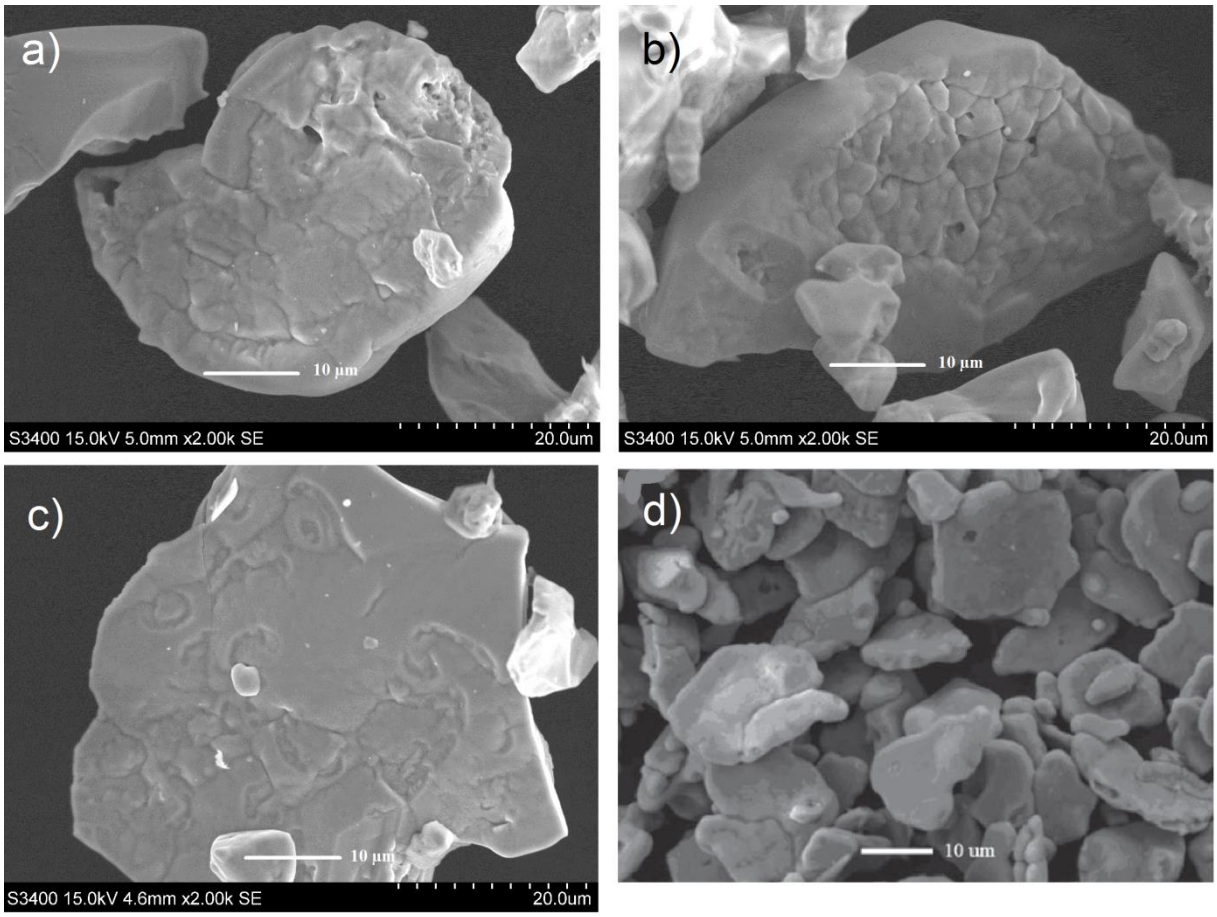

Figure 4.2: BCT powder batches, a) BCT batch 1 prepared at 1170°C for 5 hours, b) BCT batch 2 prepared at 1150°C for 5 hours c) BCT batch 3 prepared at 1170°C for 5 hours d) BT prepared by Lv *et al.* [22]

Table 4.2: Calculated aspect ratios for the synthesised BCT templates.

BCT batch number	Conversion temperature (°C)	Conversion time (h)	Diameter (µm)	Thickness (µm)	Aspect ratio
1	1170	5	22 – 49	3.5 – 7	3 – 17
2	1150	5	21 – 44	6 – 8	2 – 8
3	1170	5	23 – 51	2 – 10	2 – 22
BT reference [22]	1170	5	10 – 20	< 1.5	7 – 14

Figure 4.3 depicts the change in appearance when converting B6T17 to BCT. In general it seems like a large amount of templates have lost their high aspect ratios and evolved into more spherical or bulky particles, thus losing their plate morphology. This phenomenon is observed in all batches.

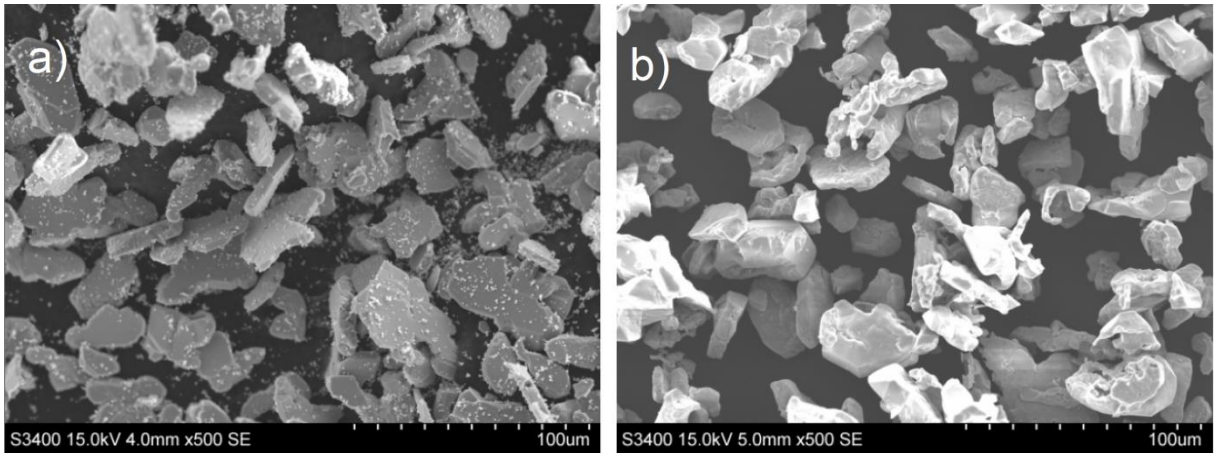

Figure 4.3: Batch 2 of prepared a) B6T17 and b) BCT. Conversion from B6T17 to BCT has left some of the particles with a geometry not resembling plates.

Figure 4.4 depicts the x-ray diffractogram of cast B6T17 batches 1, 2 and 3, while Figure 4.5 depicts the x-ray diffractogram of dry B6T17 batches 1, 2 and 3. In Figure 4.5 some $BaTiO_3$ impurities are observed. Figure 4.6 depicts the x-ray diffractograms of the cast BCT batches, while Figure 4.7 depicts the dry BCT batches. Figure 4.6 indicates the presence of a secondary phase in BCT batch 2. The difference in diffraction intensities in Figures 4.6 and 4.7 are caused by the textured template powder. When the templates are cast in ethanol the face of the platelets parallel to the (111) plane (in the case of BCT) are diffracted to a larger degree than other directions in the perovskite crystal. This leads to a higher diffracted intensity for the (111) plane. The same explanation is applicable to the B6T17 templates regarding the (100) planes. Table 4.3 shows the calculated Lotgering factors with respect to the (111) plane, calculated from diffractograms in Figure 4.6 and Figure 4.7.

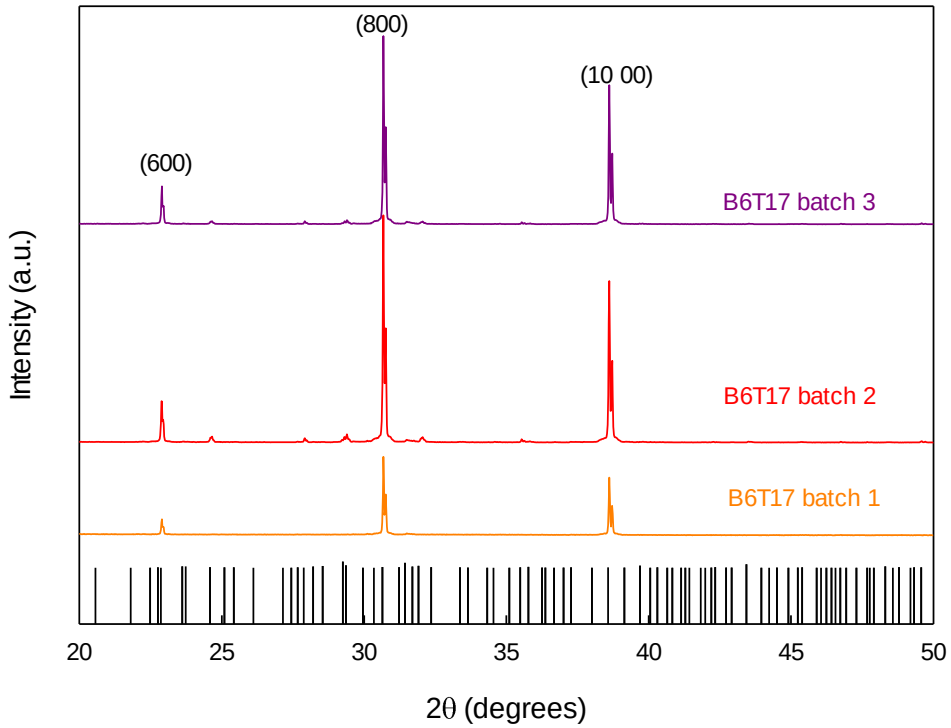

Figure 4.4: X-ray diffractograms of cast B6T17 batches. All batches were prepared at 1150°C for 3 hours. Reference PDF: 01-073-5502, $Ba_{11}Ti_{28}O_{66.5}$.

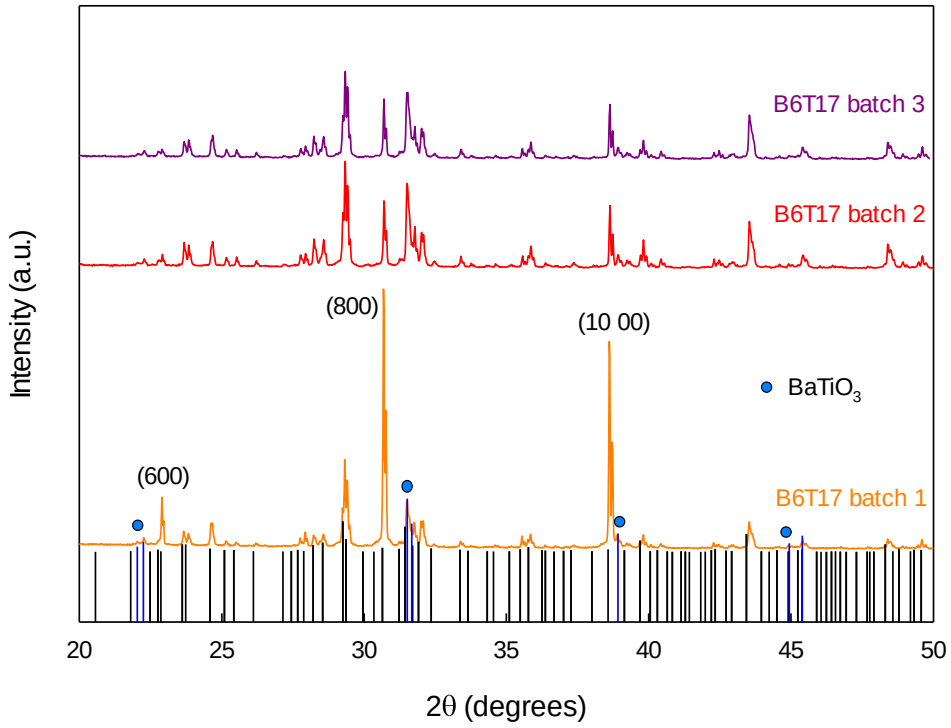

Figure 4.5: X-ray diffractograms of dry B6T17 batches. All batches were prepared at 1150°C for 3 hours. Reference PDF's: 01-073-5502, $Ba_{11}Ti_{28}O_{66.5}$, and 01-074-2491, $BaTiO_3$.

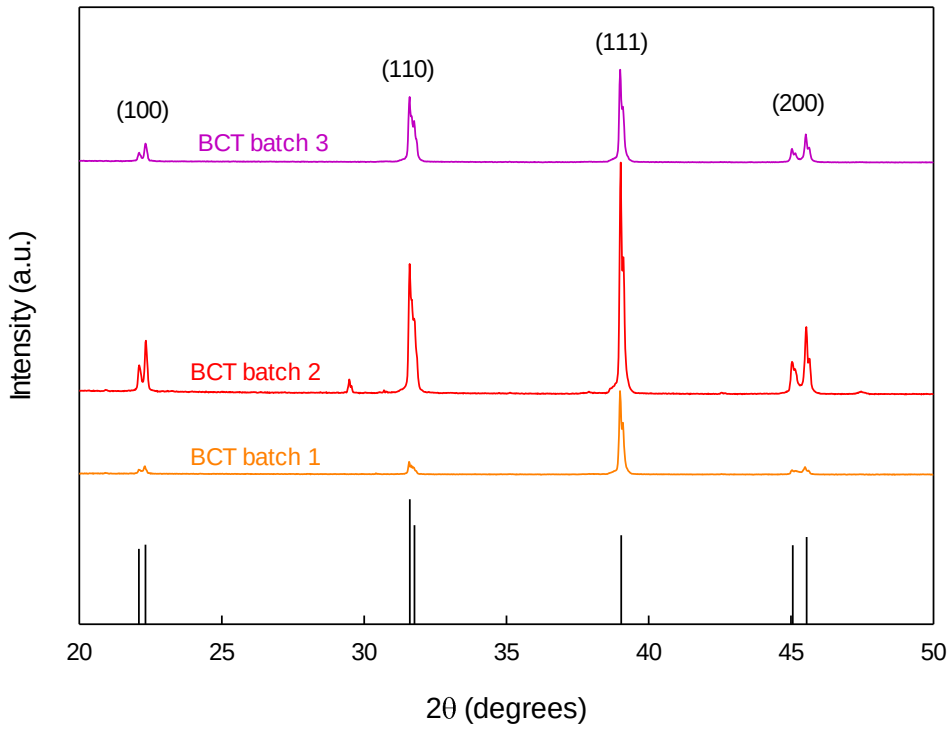

Figure 4.6: X-ray diffractograms of cast BCT batches. Batch 1 and 3 were prepared at 1170°C for 5 hours, and batch 2 at 1150°C for 5 hours. Reference PDF: 04-006-0819, $Ba_{0.93}Ca_{0.07}TiO_3$.

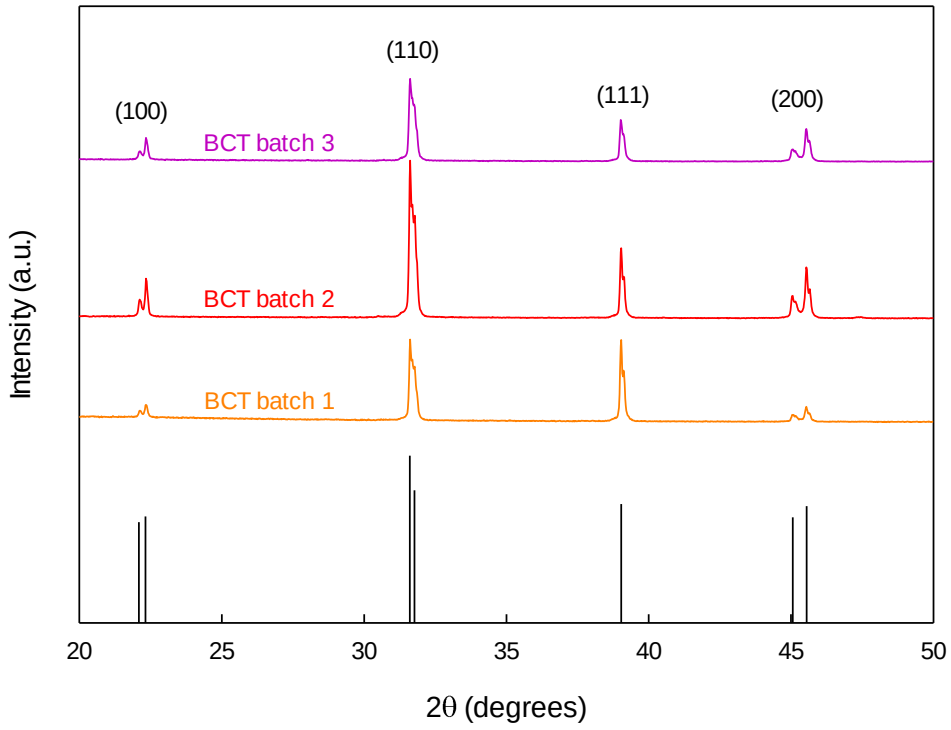

Figure 4.7: X-ray diffractograms of dry BCT batches. Batch 1 and 3 were prepared at 1170°C for 5 hours, and batch 2 at 1150°C for 5 hours. Reference PDF: 04-006-0819, $Ba_{0.93}Ca_{0.07}TiO_3$.

Table 4.3: Calculated F_{111} for BCT powder batches 1-3.

BCT batch	Preparation	F_{111} (%)
1	Dry	25.2
1	Cast	59.4
2	Dry	4.6
2	Cast	30.8
3	Dry	5.6
3	Cast	29.1

4.2 Tape characterisation

BCT batch 1 had an F_{111} of almost 60% (cast), making this the preferred choice for use in tape casting. BCT batch 1 was used in tapes 1, 2 and 3, while BCT batch 3 was used in tape 4 as BCT batch 3 had the same F_{111} as BCT batch 2, but had fewer impurities, see Figure 4.6. Table 4.4 lists relevant tape casting parameters for each tape. An unrealistically high F_{111}=25.4% is observed in tape 2, considering that the total Lotgering factor for the green tape cannot exceed the total volume of templates added to the slurry, i.e. 10%. This is probably caused by insufficient mixing during slurry preparation, causing an inhomogeneous distribution of BCT templates in the tape.

Table 4.4: Tape casting parameters, resulting thickness and F_{111}.

Tape number	BCT batch	Matrix BCT batch	Template/ Matrix ratio	Casting speed (cm/min)	Average tape thickness (µm)	F_{111} (%)
1	1	288	10/90	5	70	8.7
2	1	288	10/90	55	50	25.4
3	1	313	10/90	55	70	13.9
4	3	313	20/80	55	100	7.6

The x-ray diffractograms of all the tapes are depicted in Figure 4.8. The first BCT matrix powders used in tape casting (denoted 288) had some impurities. A second batch (denoted 313) with less impurity was therefore used in the remaining two tapes, to minimise the effects of unwanted impurities. Both batches were identified by EDS to contain Al [30]. The extra peaks in Figure 4.8 are therefore likely to be an Al-containing secondary phase. However, characterisation of these impurities was not the focus of the present work. Figure 4.9 depicts the fracture surfaces of all the tapes after they were fractured while immersed in liquid nitrogen. Other fracturing techniques resulted in slightly plastically deformed fracture surfaces which are not included in this rapport.

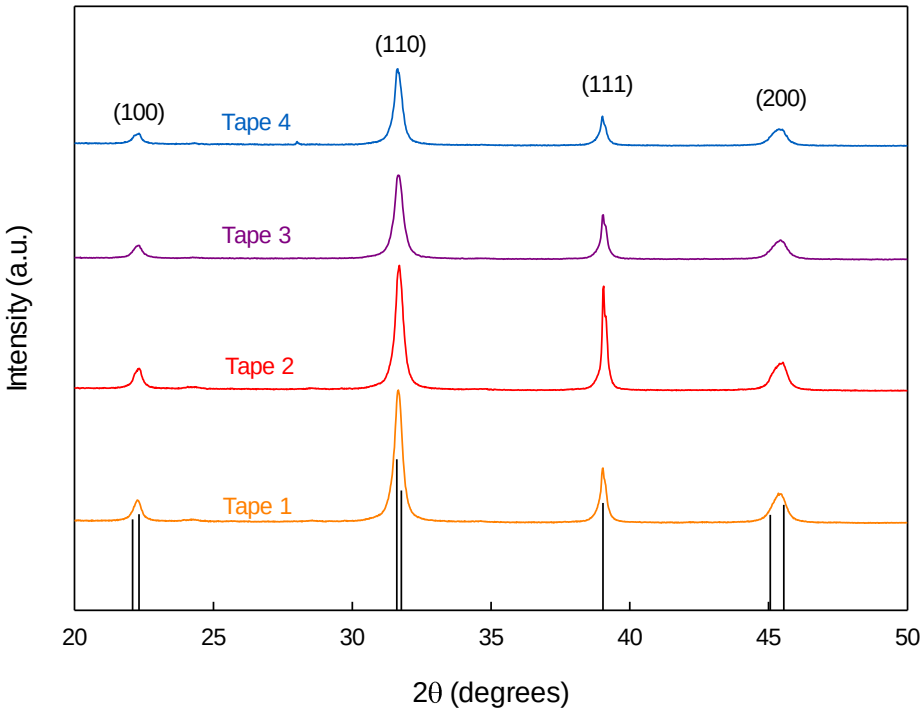

Figure 4.8: X-ray diffractograms of green tapes 1-4. Reference PDF: 04-006-0819, $Ba_{0.93}Ca_{0.07}TiO_3$.

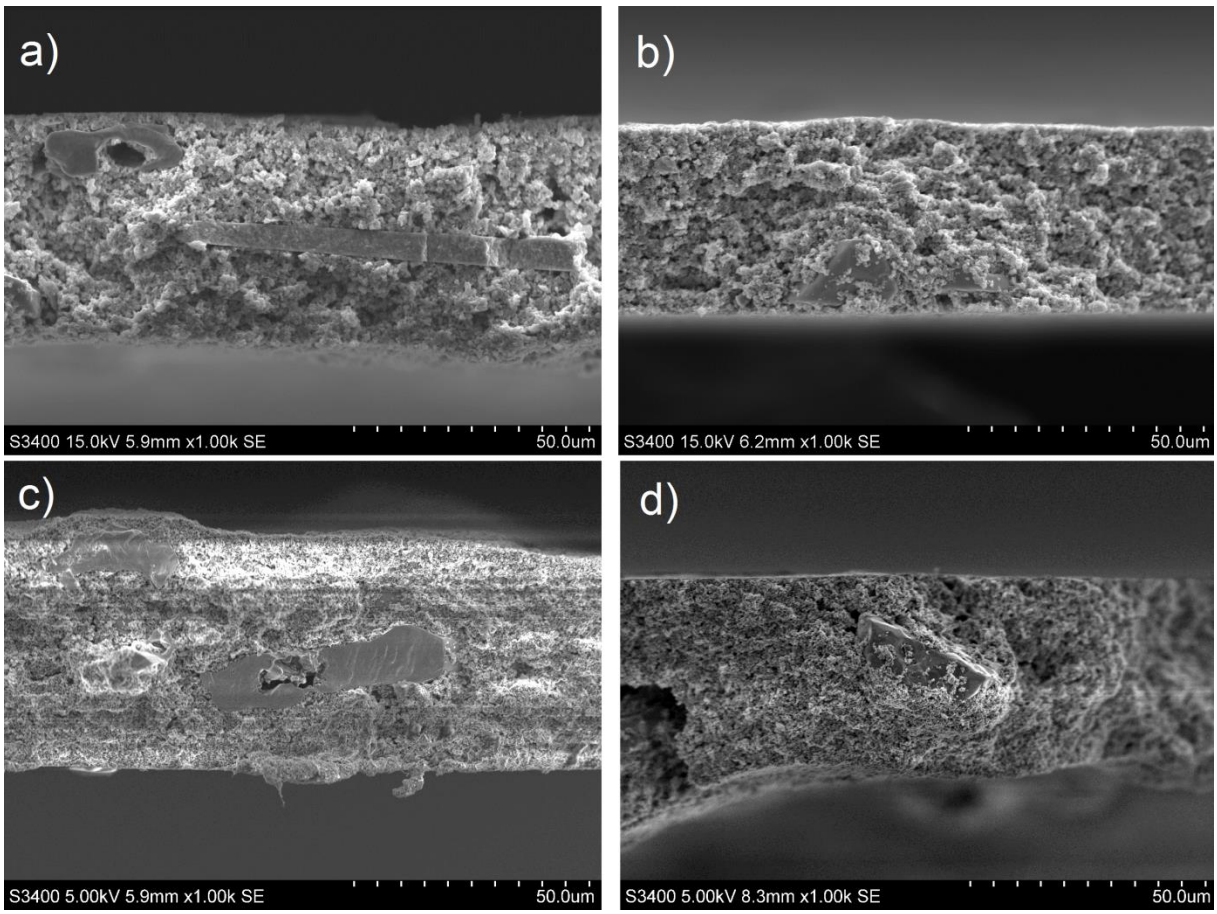

Figure 4.9: SEM micrographs of tape cross sections after fracture while immersed in liquid nitrogen to promote a brittle fracture: a) tape 1 b) tape 2 c) tape 3 d) tape 4.

4.3 Characterisation of sintered laminates and pellets

All laminate x-ray diffractograms are depicted in Figure 4.10 and all pellet diffractograms in Figure 4.11. Table 4.5 lists preparation parameters and resulting densities and F_{111} of the prepared laminates. Table 4.6 lists the preparation parameters for pellets as well as densities and F_{111} values. Figure 4.12 illustrates the correlation between F_{111} and density for the textured laminates. Figure 4.13 shows cross sectional pictures of all laminates. Pores visible in f) are elongated, perpendicular to the stacking direction and separated by a thickness corresponding to the tape used. Figure 4.14 depicts all laminate surfaces. In Figure 4.14 a), b), c) and f) secondary phase is visible as elongates grains on the surface. Matrix grain size varies in Figure 4.14: a), b) and c) have larger matrix grains than d), e) and f). Template grains ranging in size from approximately 20-50 µm are visible in all laminates, and are more rounded compared to the BCT templates in Figure 4.2.

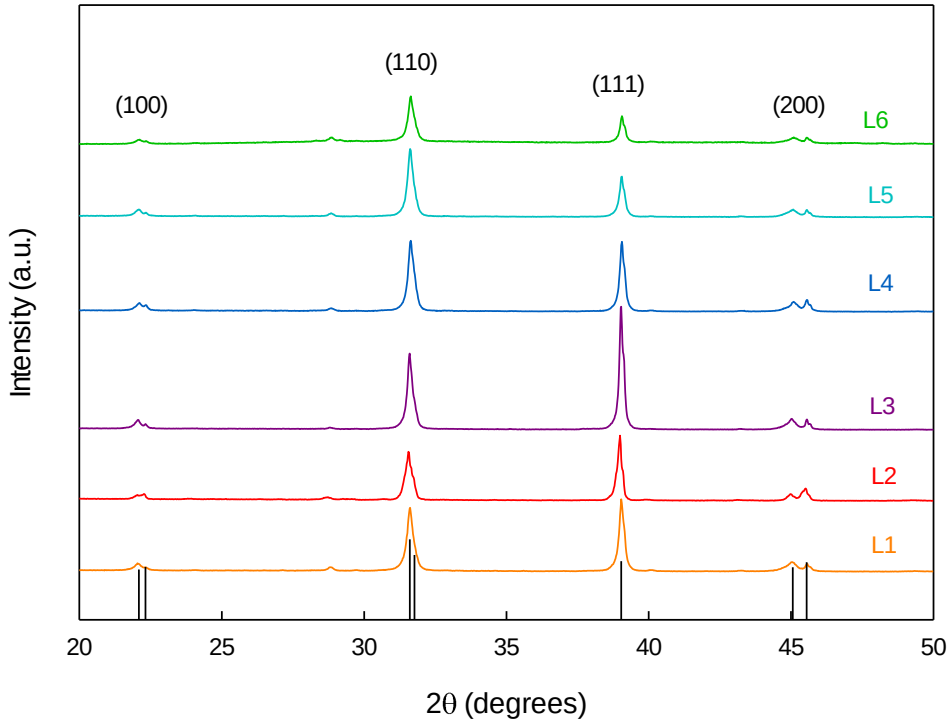

Figure 4.10: Laminate x-ray diffractograms. Reference PDF: 04-006-0819, $Ba_{0.93}Ca_{0.07}TiO_3$.

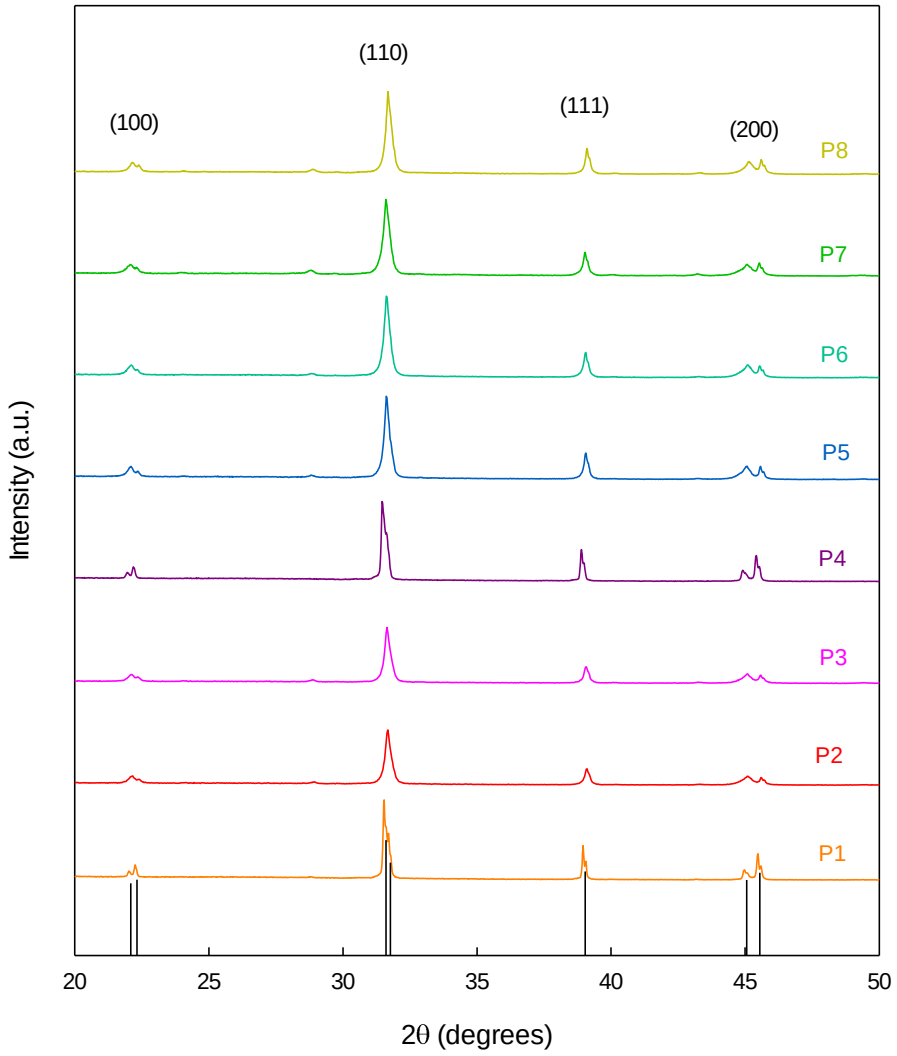

Figure 4.11: Pellet x-ray diffractograms. Reference PDF: 04-006-0819, $Ba_{0.93}Ca_{0.07}TiO_3$.

Table 4.5: Laminate preparation parameters, resulting densities and F_{111}.

Sample name	Made from tape no.	Number of stacked squares	Size (cm x cm)	Laminating pressure (MPa)	Sintering temp. (°C)	Density (%)	F_{111} (%)
L1	1	27	1.5 x 1.5	30	1350	88.2	32.1
L2	1	27	1.5 x 1.5	30	1300	87.8	33.7
L3	2	60	1.5 x 1.5	40	1350	93.4	42.7
L4	3	43	1.5 x 1.5	40	1350	91.3	27.5
L5	4	30	1.5 x 1.5	40	1350	85.0	16.6
L6	4	30	1.0 x 1.0	45	1350	81.9	13.5

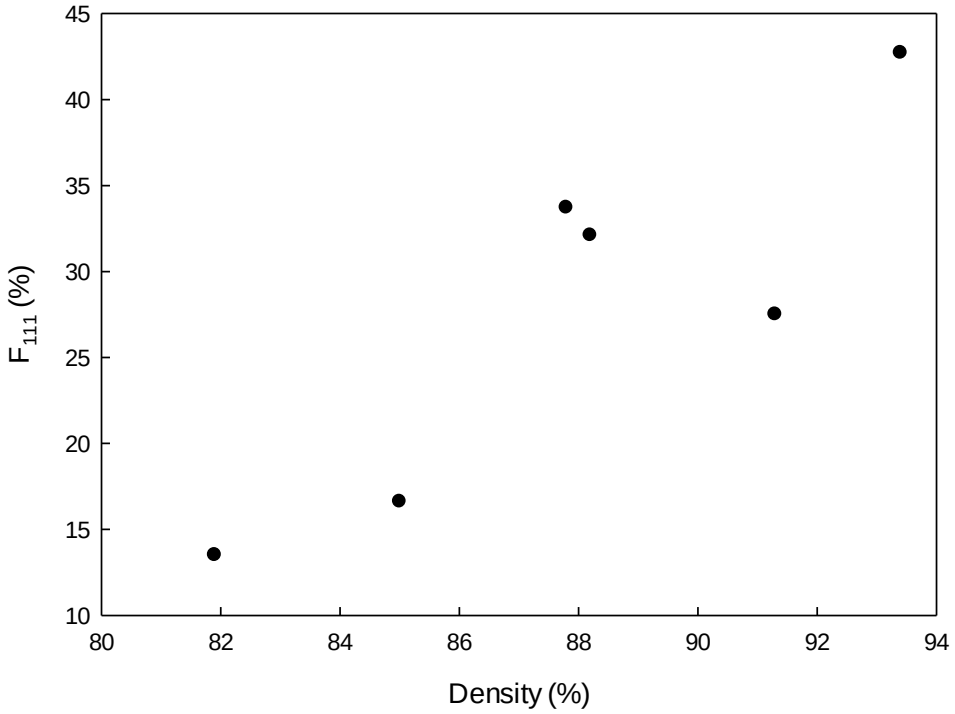

Figure 4.12: Texture (F_{111}) versus density for laminates.

Table 4.6: Pellet preparation parameters, resulting densities and F_{111}.

Sample name	Matrix powder	Pressure (MPa)	Sintering temp. (°C)	Density (%)	F_{111} (%)
P1	288	120	1350	91.8	4.7
P2	288	120	1350	91.8	0.3
P3	288	110	1300	89.3	0.0
P4	288	110	1300	90.3	3.4
P5	288	110	1350	92.1	1.5
P6	313	110	1350	91.7	1.6
P7	313	110	1350	87.6	0.9
P8	313	110	1350	86.3	1.2

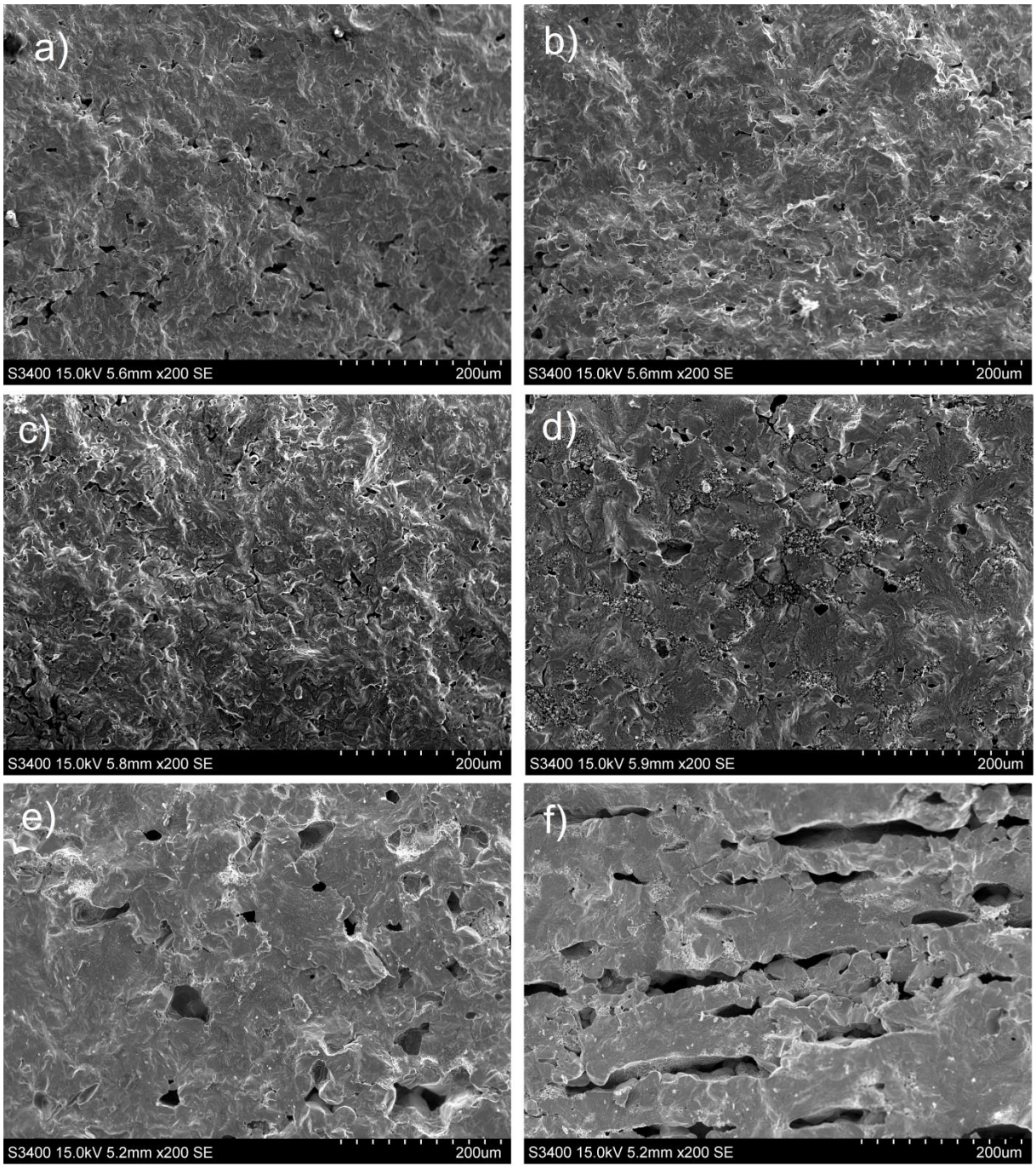

Figure 4.13: Micrographs showing cross sectional view of a) L1, b) L2, c) L3, d) L4, e) L5 and f) L6. The image horizontal axis is perpendicular to the stacking direction.

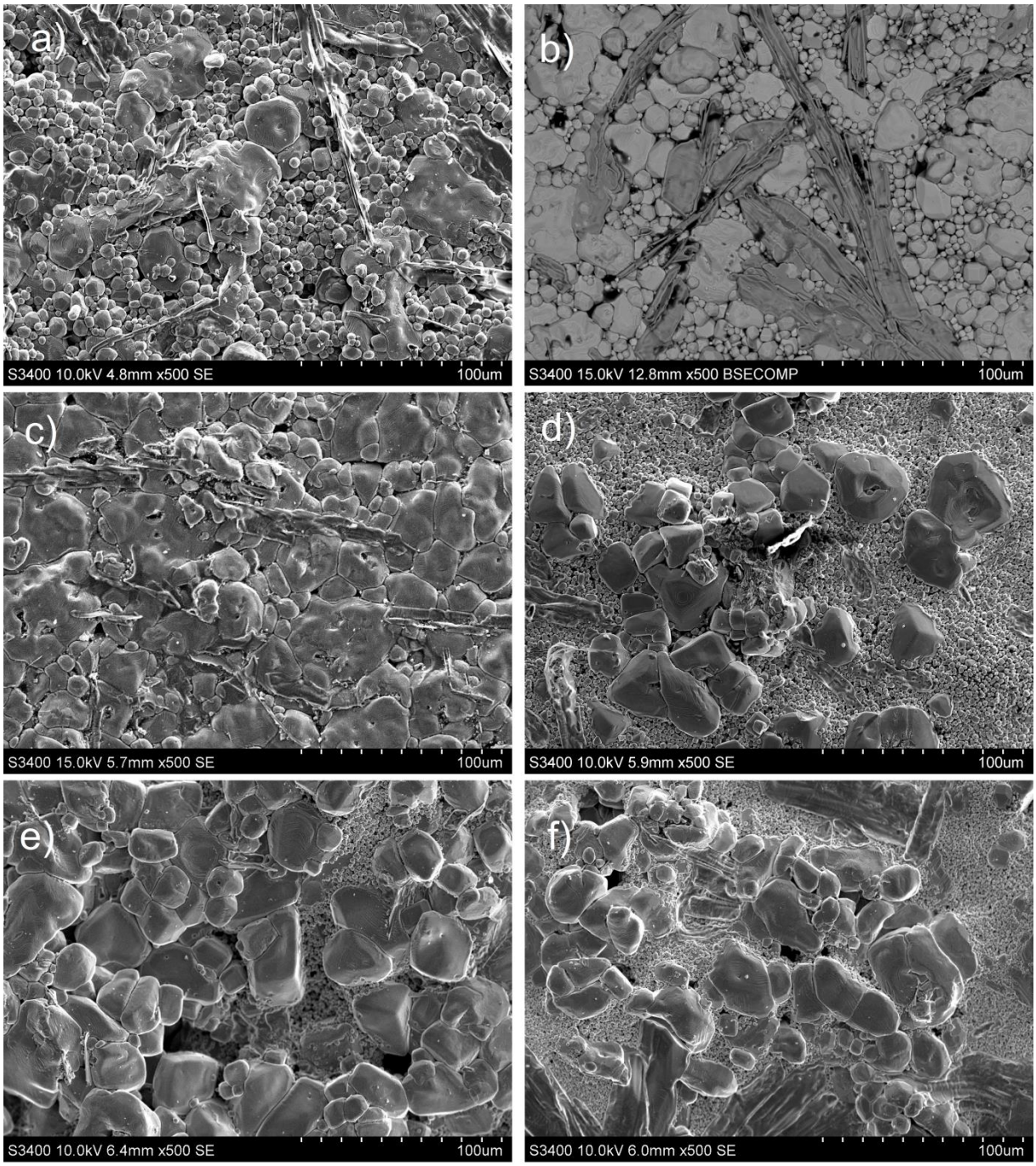

Figure 4.14: Micrographs of surfaces of a) L1, b) L2 depicted in backscattered mode with visible secondary phase present as elongated grains, c) L3, d) L4, e) L5 and f) L6.

4.4 Piezoelectric characterisation

The laminates with density above 90% used for piezoelectric characterisation are listed in Table 4.7. Results of converse and direct d_{33} measurements are also listed. The converse d_{33} values are calculated by the piezo software with an approximation that tends to overestimate the values. This should be kept in mind when comparing the two coefficients. Samples with densities below 90% were not used for piezoelectric characterisation, as the large fraction of pores in the material is expected to increase conductivity and lead to detrimental leakage current. The pellets which are relevant for testing are P5 (same sintering program and matrix powder (288) as L3) and P6 (same sintering program and matrix powder (313) as L4).

Figure 4.15 and Figure 4.16 show the hysteresis curves of L3 and P6, respectively. L4 is depicted in Figure 4.17 first at a low field (5 $kVcm^{-1}$) where there is some ferroelectric hysteresis behaviour, and then at higher field (20 $kVcm^{-1}$) where resistor behaviour is dominating. Figure 4.18 shows the immediate resistor behaviour observed for P5. This resistor behaviour is caused by leakage currents in the samples and resulting polarisation versus field plots are therefore different from the hysteresis loops in Figure 4.15 and 4.16.

Figure 4.19 depicts the current as a function of the electric field along with a graph of the applied voltage for L3 and P6. The characteristic butterfly loop for samples L3, L4 and P6 is seen in Figure 4.20, where strain versus bipolar electric field is plotted. Strain versus unipolar electric field for L3, L4 and P6 is shown in Figure 4.21. Figure 4.22 depicts the converse d_{33}-values versus applied electric field. Values were calculated by the aixPES software from the slope of the strain curves in Figure 4.21. P5 is not included in Figures 4.20-4.22 because of its resistor behaviour, making it incomparable with the other results.

Table 4.7: Laminates and pellets used in piezoelectric characterisation with measured piezoelectric coefficients.

Sample	Density (%)	F_{111} (%)	Area (mm^2)	Thickness (mm)	Aspect ratio	Converse d_{33} (pmV^{-1}) at 20$kVcm^{-1}$	Direct d_{33} (pCN^{-1}) after testing
L3	93.4	42.7	132.93	0.97	13.7	143	49±3
L4	91.3	27.5	83.86	0.83	10.1	18	28±3
P5	92.1	1.5	52.39	2.21	2.4	-	0
P6	91.7	1.6	53.69	1.72	3.1	36	43±4

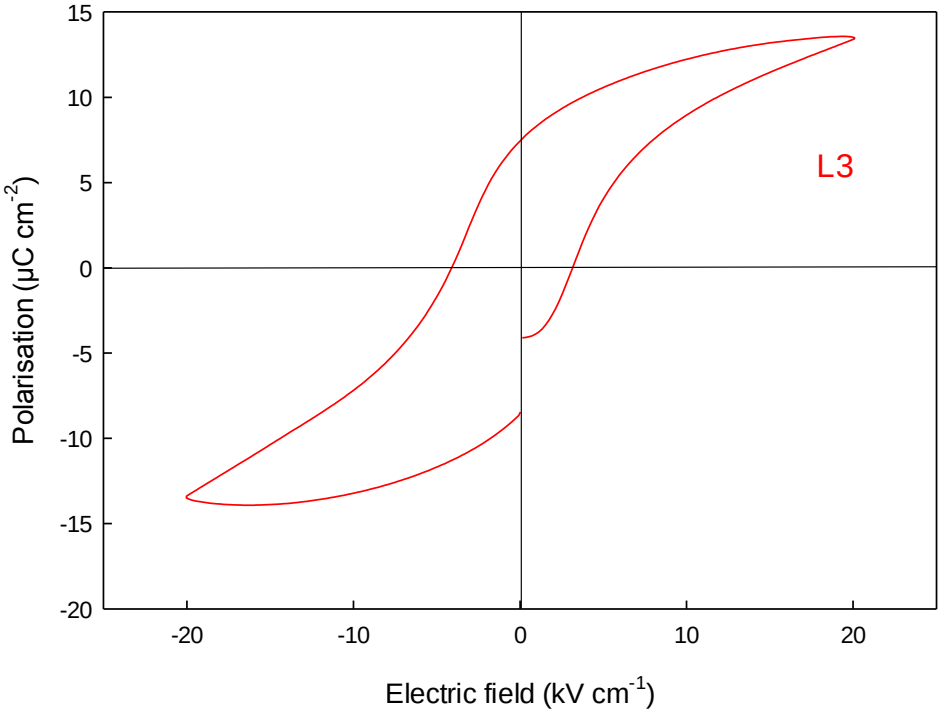

Figure 4.15: Polarisation hysteresis loop for L3.

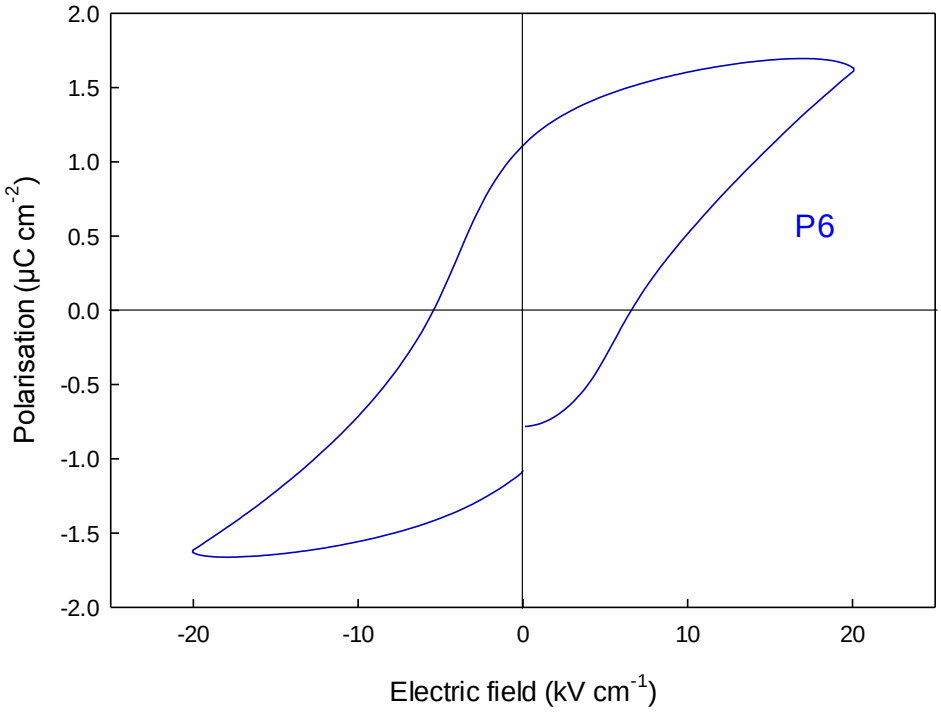

Figure 4.16: Polarisation hysteresis loop for P6.

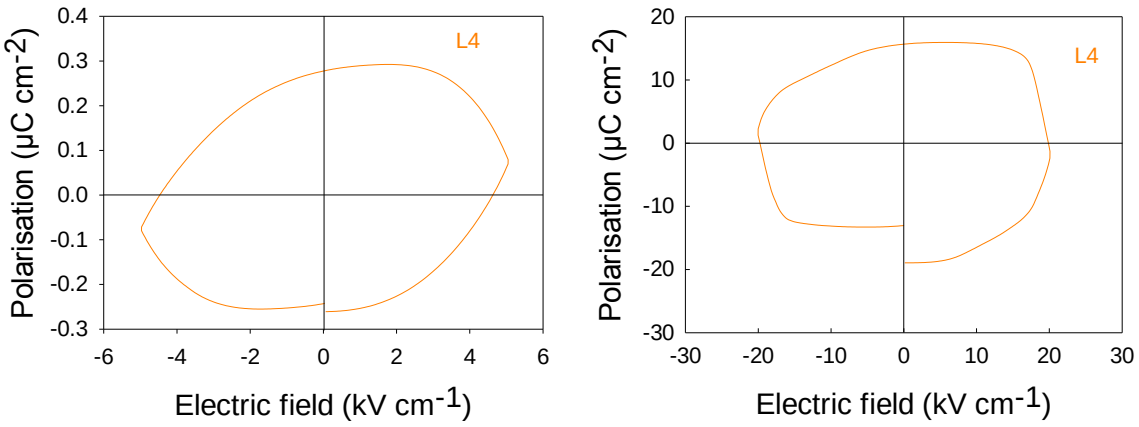

Figure 4.17: Polarisation curves for L4. Increasing field strength gradually increases resistor behaviour.

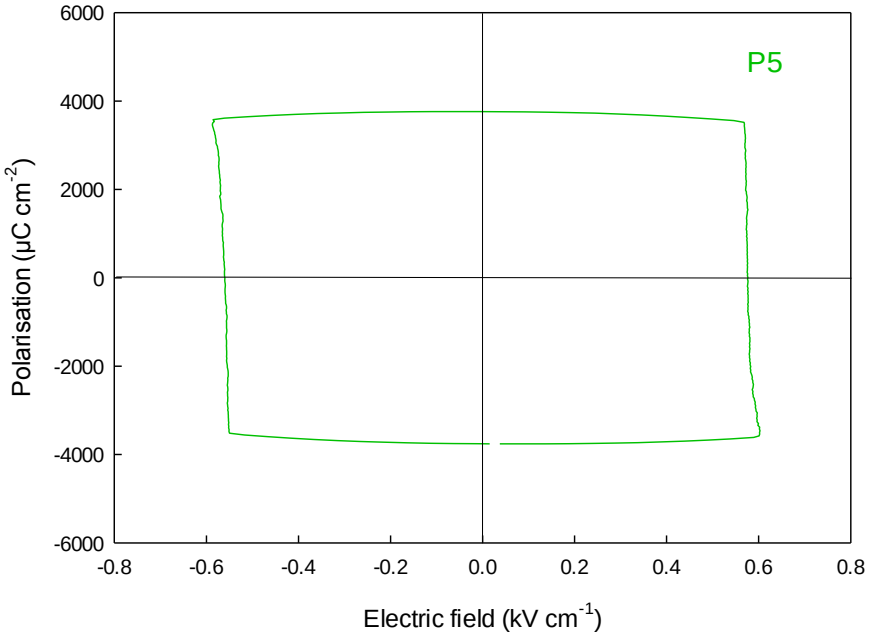

Figure 4.18: Polarisation curve for P5 showing immediate resistor behaviour.

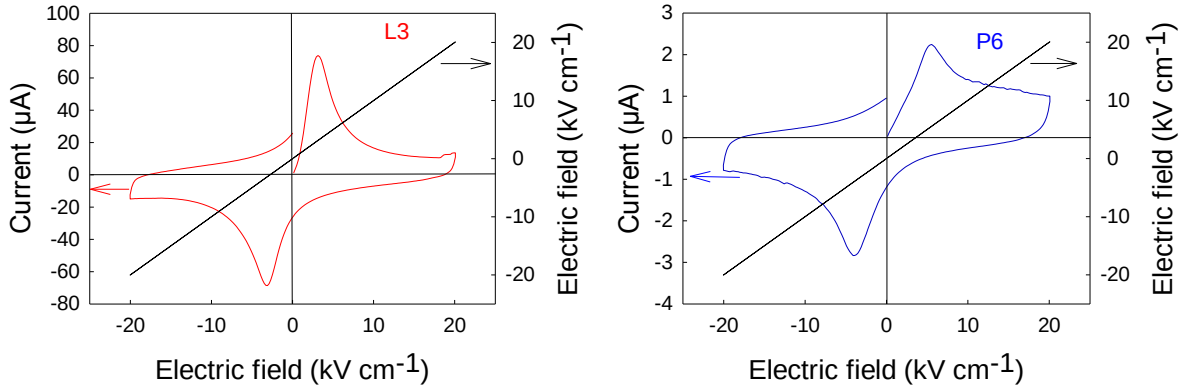

Figure 4.19: Current as a function of electric field for L3 and P6. The black diagonal line indicates the applied voltage.

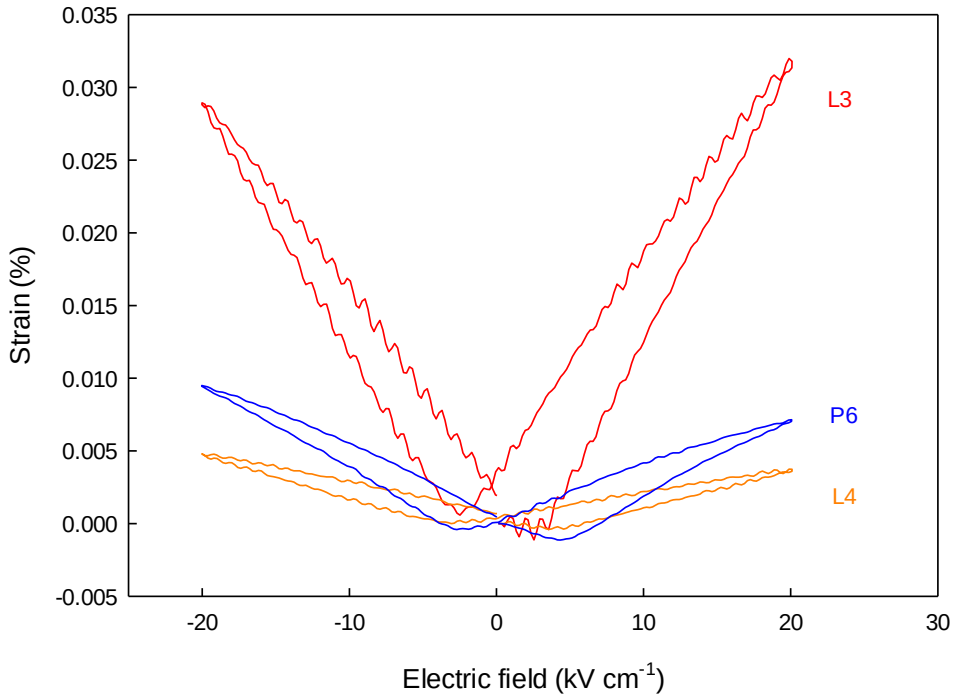

Figure 4.20: Strain versus electric field (bipolar) showing characteristic butterfly loop for piezoelectric materials L3, L4 and P6.

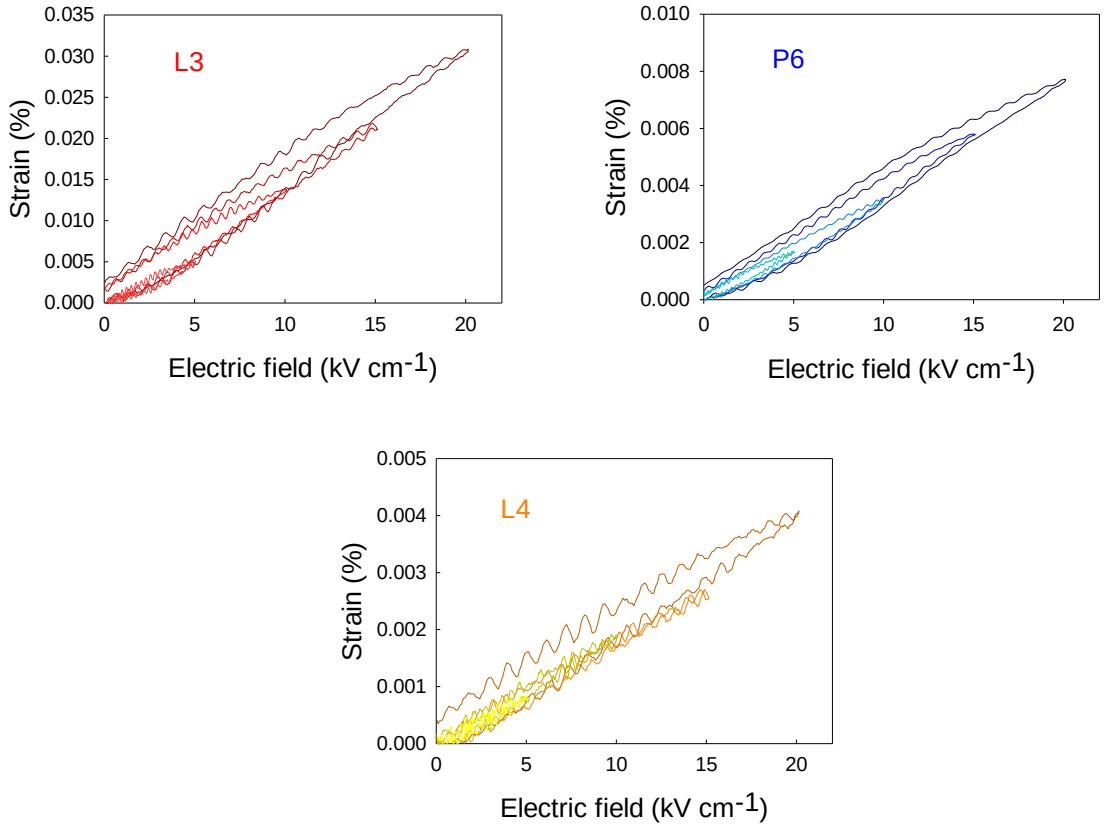

Figure 4.21: Strain versus electric field (unipolar) for the laminates L3, L4 and the reference pellet P6. Note large differences in max strain values.

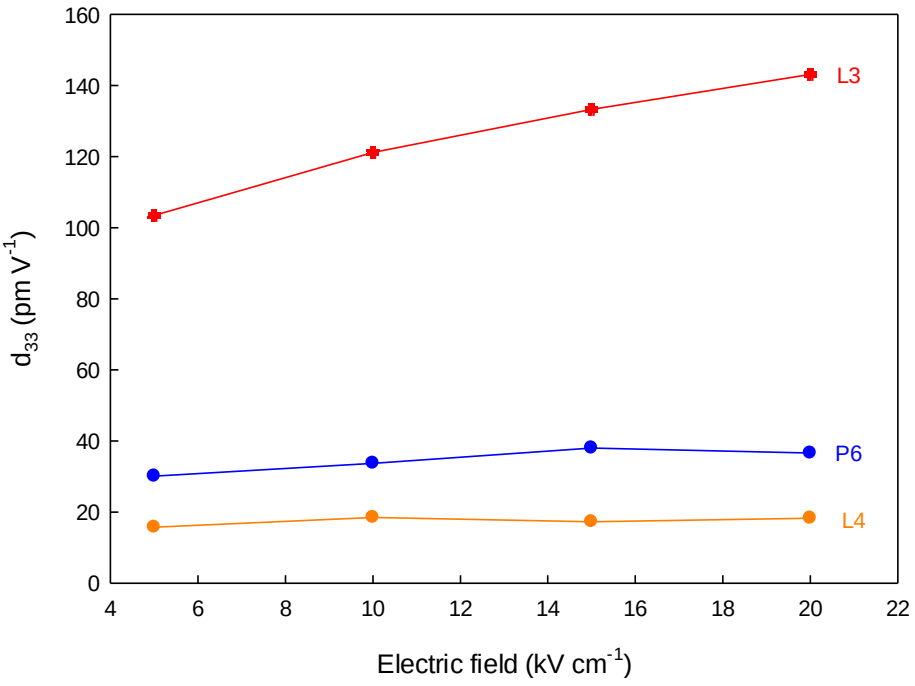

Figure 4.22: Average converse d_{33}-values versus electric field. Converse d_{33}-values are estimated from strain curves in Figure 4.21, by aixPES software.

5. Discussion

5.1 Template morphology

There are distinct differences between templates prepared in the present work and templates prepared by Lv *et al.* [22] First of all the B6T17 diameters obtained are larger, as can be seen in Table 4.1. However because of the templates being thicker as well, the resulting aspect ratios are somewhat lower. The difference in obtained template size may have been caused by different reactant powder particle sizes, or by different mixing techniques of reactants. BT and TiO_2 were mixed in a ball mill by Lv *et al.* while reactants in the present work were mixed using a mortar. Synthesis temperatures may also have been slightly different because of local furnace variations.

Figure 4.2 depicts synthesised BCT templates which, compared with the BT templates synthesised by Lv *et al.* [22] are fairly large, and thick. The second batch of BCT was prepared at 1150°C instead of 1170°C, in an attempt to decrease the template thickness. However, as is clear from Table 4.2, lowering the conversion temperature did not decrease template thickness. Perhaps a more drastic decrease in temperature or alternatively a shorter holding time would have decreased the template thickness, while still retaining the template diameter and thus increasing the aspect ratio.

When comparing the surface structure of the B6T17 templates in Figure 4.1 and the BCT templates in Figure 4.2 an increased roughness in the converted BCT templates can be observed. This is probably caused by the mechanism of the topotactic conversion process as described in Chapter 2.4. Because growth initiates at multiple point on the B6T17 surface and the B6T17 layered structure starts to exfoliate, a more uneven surface, consisting of highly oriented crystallites is formed.

From Figure 4.3 it is clear that the topotactic conversion process has not been completely successful in retaining the desired template morphology. This might have been caused by excessive crushing of the B6T17 templates during mixing before the conversion took place. Another explanation could be that the reactants were not mixed to a homogeneous mixture leading to slightly different reactions taking place at different places in the crucible. This lack of plate like morphology will have a negative impact on the orientation, and should therefore be optimised further.

5.2 Template orientation and purity

Figure 4.4 gives a strong indication of the presence of a dominant (100) plane in the prepared B6T17 templates. This same orientation is also visible in Figure 4.5, although to a lesser degree. This is caused by differences in sample preparation as mentioned earlier. Powder used for the diffractogram in Figure 4.4 was cast in ethanol while powder used for Figure 4.5 was dry.

As indicated by the figure captions of both Figure 4.4 and Figure 4.5, the most accurate match to the diffraction patterns is $Ba_{11}Ti_{28}O_{66.5}$ and not the expected $Ba_6Ti_{17}O_{40}$. This $Ba_{11}Ti_{28}O_{66.5}$ ceramic has a Ti:Ba ratio between B6T17 and $BaTi_2O_5$ which is found on the BaO-rich side in the BaO-TiO_2 phase diagram in Figure 2.5. The fact that the B6T17 synthesis seems not to have reached completion with respect to adding sufficient amounts of TiO_2 to the templates is not unexpected because of the excess Ba added to avoid formation of $Ba_4Ti_{13}O_{30}$. Adding less Ba in excess during precursor synthesis would likely result in the desired B6T17 stoichiometry. Even though the precursor templates seem to be of a slightly different Ti:Ba ratio, the conversion from B6T17 to BCT has still led to a certain degree of (111) orientation as desired. Depending on the structure of the $Ba_{11}Ti_{28}O_{66.5}$ phase detected, this phase could also have some orientation relationship to BCT, making a topotactic conversion possible. However, this possible orientation relationship has not been investigated in the present work. It is therefore unclear whether reaching the exact B6T17 stoichiometry would actually increase the degree of orientation of the converted BCT templates or not. This should be investigated further, by trying to synthesise phase pure B6T17.

The diffractogram in Figure 4.5 also indicates some secondary phase consisting of unreacted $BaTiO_3$. Again, this is coherent with the fact that an excess of Ba was added to avoid formation of $Ba_4Ti_{13}O_{30}$. According to Lv *et al.* [22] who did EDS analysis, the small white particles attached to the B6T17 template surfaces, which can be seen in Figure 4.1 d), were identified as unreacted $BaTiO_3$. The B6T17 depicted in Figure 4.1 a)-c) also has some unidentified white particles, which therefore is assumed to be unreacted $BaTiO_3$.

The converted BCT batches are mostly phase pure, although a small peak around $2\theta=30°$ in batch 2 is visible in the diffractogram of cast templates (Figure 4.6). However, this peak is not visible in the dry samples (Figure 4.7) indicating that the impurity may be a result of poor sample preparation. The degree of orientation for BCT varies between batch 1 and batch 2 and 3. As is visible from Figure 4.6 and Table 4.3, the first BCT batch has an F_{111} (cast) of close to 60%, while the other two batches have an $F_{111}\approx$ 30%. It is unclear why batches 2 and 3 have a much lower F_{111} than batch 1. It might be caused by slightly different preparation procedures. For examples batches 2 and 3 were converted with a 10wt% reduced batch size. However, it is unlikely that this would have had a big effect. Comparing F_{111} values in Table 4.3 for cast and dry samples again underscore the difference in diffraction intensities for aligned templates (cast) and randomly oriented templates (dry).

5.3 Tape casting

Table 4.4 seems to indicate a drastic increase in F_{111} by increasing casting speed when comparing tape 1 and 2. However, as tape 2 was prepared in a way that resulted in a very inhomogeneous distribution of templates in the tape, it is likely that the segment of tape chosen for XRD, by chance contained a higher concentration of templates, compared to other segments of this same tape, and thus led to an apparently high F_{111}. When adding 10% templates to a slurry, it is not theoretically possible for the tape to have a degree of orientation exceeding 10% if the templates are distributed evenly throughout the tape. This is why this

high value of 25.2% most likely is caused by inhomogeneously distributed templates. Tape 3 on the other hand is made from a slurry which had a more homogeneous distribution of templates. The F_{111}=13.9% is therefore a more realistic representative of the entire tape. It should be noted that because of slight mechanical losses during slurry preparation a slightly higher amount than 10wt% of templates was added.

To investigate the effects of casting speed on template orientation, the F_{111} of tape 1 and 3 are compared. Increasing casting speed seems to have increased the orientation of the added templates going from 8.7% to 13.9%. However this could also be caused by random variations in the tapes and inhomogenously distributed templates. The effect of tape casting speed is therefore not clearly observed.

The fourth tape has a significantly decreased F_{111} possibly owing to multiple factors, the main factor being use of BCT batch 3 which has an F_{111} of only 29.1% compared to batch 1 with F_{111} of 59.4%. Other dissimilarities between tape 4 and the other tapes is the amount of templates, which was increased to about 20wt% instead of 10wt%. Also the amount of dry constituents in the slurry is considerably larger in tape 4, making the slurry more viscous. Both of the latter factors regarding template amount and slurry viscosity should in theory have led to an increase in orientation and consequently F_{111} because of the increase in shear forces aligning templates. It seems however that the increase in shear forces is not enough to outweigh the low F_{111} of BCT batch 3. A too high template content can generally decrease texture in a material because of restrictions in template movement, however at 20wt% this limit is probably not reached.

Template alignment within the tape cast plane can be observed visually by micrographs depicted in Figure 4.9. The larger templates like the one in Figure 4.9 a) and c) seem to be more easily aligned than the smaller templates like the ones depicted in b) and d). This seems plausible as the greater the surface area of the template, the greater the effect of shear forces on the template.

5.4 Density and texture of samples

Table 4.5 lists the important characteristics for each laminate. To determine the optimal sintering temperature, the two first laminates L1 and L2 were sintered at 1350°C and 1300°C, respectively. Although the difference in achieved density was quite small, (L1=88.2%, and L2=87.8%) sintering at 1350°C seems to give the best density and was thus the chosen sintering temperature. To improve the density of the laminates, the laminating pressure was increased from 30 to 40 MPa. This gave a marked increase in density for L3 and L4 with 93.4% and 91.3% densities respectively. L5 and L6 have the lowest densities, and are depicted in Figure 4.13 e) (L5) and f) (L6) with a cross sectional view. The large elongated pores between layers in L6 are the main causes of low density. This is probably caused by a poor lamination procedure as the sintering within each tape is dense and the areas between the tapes are porous. Table 4.5 indicates a slightly higher pressure was used when laminating L6 (P=45 MPa), making the large pores slightly unexpected. However, the actual applied

pressures are highly variable as it is difficult to apply the exact same pressure with the hot press equipment.

A correlation between density and texture is shown in Figure 4.12. Because template growth is restricted by the presence of pores in the structure, eliminating pores and increasing density is paramount to achieving a high degree of texture in the material. The highest density achieved in the present work was 93.4% (L3), indicating that the rapid growth regime, mentioned in Chapter 2.4, has not been reached. Even so there seems to be a correlation between the presence of pores and the template growth even before the rapid growth stage at 95% density is reached. Previous attempts at texturing similar systems (BT) have reported F_{111} from 27% [15] to 79% [33]. Maximum texture achieved in the present work is 42.7%. As expected, the non-textured pellets have very low F_{111} compared to textured laminates. Variations in texture for the pellets are attributed to random individual differences.

Figure 4.14 b) shows the secondary phase formed on the surface of L2. Similar elongated phases were formed on most of the laminates, probably because of impurities introduced by the matrix powder. These secondary phases were not identified, and seem to disappear when polishing the surface, as they were not detected in backscattered mode of the polished surfaces. Some colour variations were observed, however this could also be due to different grain orientations within the BCT phase. To determine whether secondary phase is present inside the sample as well as on the surface, EDS analysis should be done on both unpolished and polished surfaces.

The surface of L3, seen in Figure 4.14 c), has very large template grains and a lower amount of small matrix grains than in any other sample. On average the grains in L3 are larger, indicating a large degree of Ostwald ripening. Each grain has a neighbouring grain along all sides, with very few pores between them. Figure 4.14 d) depicts L4 which has very large template grains spread in a matrix of very fine grained matrix powder. Comparing the matrix powder in the three first laminates to the three last indicate that matrix batch 288 has larger grain size than batch 313. Some of the template grains in L4, L5 and L6 have a more cubic morphology. When template growth is impinged in the fast growing x-y direction, the growth will continue in the slow growing z-direction, resulting after time in more cubic morphologies [15]. This seems particularly to be the case for L5 where there are many close neighbouring large template grains.

5.5 Piezoelectric characterisation

Table 4.7 lists laminates and pellets which were piezoelectrically characterised. The highest direct d_{33}-value measured was 49 ± 3 pCN^{-1} and belongs to L3 which also had the highest density and $F_{111,}$ 93.4% and 42.7% respectively. L3 also had the highest converse d_{33}=143 pmV^{-1}, which is much higher than the direct d_{33}. As mentioned, this difference between direct and converse d_{33}'s is caused by the aixPES software, which overestimates the converse d_{33} from unipolar strain data. Both converse and direct d_{33}-values are low compared to reported values with similar texturing degrees of $BaTiO_3$ where a direct d_{33} of 270 pCN^{-1} has been

reported [15]. The non-textured reference pellet P6 has a direct d_{33} of 43 ± 4 pCN^{-1} which is almost as high as for the textured laminate L3. One would maybe expect the difference between d_{33} for a textured material and a non-textured material to be greater, however it must be kept in mind that the samples were not poled, making it possible for L3 to achieve a much higher d_{33} than P6 if poled correctly. This is also indicated by Figure 4.22 were the converse d_{33} measured during testing is increasing for L3, while stagnant for P6. If samples had been poled at, e.g. 80 $kVcm^{-1}$ for 20 minutes, the direct d_{33} would probably have been higher.

L4 has a lower direct d_{33} of 28 ± 3 pCN^{-1} probably due to the increasing resistor behaviour with increased field as shown in Figure 4.17. At very low fields (5 $kVcm^{-1}$) the polarisation curve shows mixed behaviour. However as the field increases (20$kVcm^{-1}$) it is clear that the current leakage causes resistor behaviour to dominate piezoelectric hysteresis behaviour. P5 showed no signs of hysteresis behaviour and was instantly showing resistor behaviour as seen in Figure 4.18. Because of this conducting behaviour the material was not polarised during testing, which was confirmed by the direct d_{33} measured after testing as seen in Table 4.7. The different behaviour of P6 and P5 are most likely caused by the random distribution of impurities in the sample. As mentioned in Table 3.3, both P5 and P6 have some colour variations on the pellet surface, indicating a slightly inhomogeneous composition, and impurities. The different colouring of P5 (brown) and P6 (grey) are most likely caused by the different matrix powder batches.

Figure 4.15 and Figure 4.16 depict piezoelectric hysteresis loops of L3 and P6, respectively. The textured sample L3 has a much higher saturation polarisation (13 μCcm^{-2}) than non-textured sample P6 (1.6 μCcm^{-2}). For L3 remnant polarisation value (P_R) is around 7 μCcm^{-2} which is low compared to values found in literature for textured $BaTiO_3$ of 28 μCcm^{-2} [15]. When texturing in the (111) plane, a decrease in polarisation is expected compared to non-textured samples. However, because of impurities these typical characteristics could be disturbed resulting in an unexpectedly low saturation polarisation for the non-textured pellet. Coercive fields for L3 and P6 are around 4 $kVcm^{-1}$ and 6 $kVcm^{-1}$ respectively, and are comparable to literature values: E_C= 5.5 $kVcm^{-1}$ for textured $BaTiO_3$ [15].

The current versus electric field plots in Figure 4.19 show some deviation from perfect ferroelectric behaviour as depicted in Figure 2.12. The gradual drop in current after the switching peak has occurred is caused by leakage currents in the material. The leakage currents occur when there are impurities or a significant amount of porosity in the material. Impurities may form conducting secondary phases which decreases the overall dielectricity of the ceramic. Pores containing air also decrease dielecticity because air is more conductive than the dielectric samples. Impurities and pores can be detrimental to a piezoelectric material if present in considerable amounts, and will lower the piezoelectric responses.

Figure 4.20 and Figure 4.21 show strain versus bipolar and unipolar fields, respectively. The magnitude of the strain response when applying a 20 $kVcm^{-1}$ field is seen in Figure 4.20. L3 has the highest strain value of about 0.03%. At similar fields strain values of 0.16% have been reported, and strain values up to 0.3% have been reported for textured BT when applying fields up to 50 kV cm^{-1} [15]. Therefore L3 has a quite weak response and is not suited for use

in actuators, where strain response should be as high as possible to maximise efficiency. L4 (0.004%) and P6 (0.008%) show even lower strain responses possibly because of earlier mentioned factors such as impurities and lower densities.

The converse piezoelectric coefficients calculated by the aixPES software are depicted in Figure 4.22. Here P6 and L4 show only slight d_{33} increase with increasing field, while L3 shows a more consistent increase going from 100 pm V^{-1} at 5 kV cm^{-1} to 140 pm V^{-1} at 20 kV cm^{-1}. At the point of saturation polarisation this increase is expected to diminish and eventually stabilise at a constant value. Therefore a higher electric field should be applied to reach the maximum converse d_{33} value, resulting in a poling of the ferroelectric and also increasing the direct d_{33}. This means that even though the d_{33} values are low compared to literature, a higher value could still be achievable if the material is poled. This is a promising result for the effect of texture on the piezoelectric response for BCT.

6. Concluding remarks and further work

In the present work, BCT templates with a (111)-orientation have been synthesised and used in a templated grain growth reaction to produce dense, textured piezoelectric ceramics with an increased piezoelectric coefficient. By using a two-step procedure, BCT templates with a F_{111}=59.4% were achieved when converting precursor templates (B6T17) in a molten salt conversion at 1170˚C for 5 hours. Large BCT templates (20-50 µm) with high aspect ratios (2-20) were achieved. SEM micrographs indicate a topotactic conversion from B6T17 to BCT. Parallel nucleation sites at the surface of the precursors lead to a facetted polycrystalline BCT template with a rough surface. The hypothesis of topotaxy between precursor and template is supported by x-ray diffractograms, indicating a $(100)_{B6T17} \parallel (111)_{BCT}$ orientation relationship. Adding an excess of Ba to the B6T17 synthesis resulted in precursor templates with a Ti:Ba ratio of 2.5, instead of 2.8. By adding less Ba in excess during precursor production, precursor template composition will approach a Ti:Ba ratio of 2.8. If the precursors have a stoichiometry closer to B6T17, the conversion could possibly be able to better utilise the topotactic relationship between B6T17 and BCT, retaining template morphology and thus increasing the overall F_{111} of the resulting BCT templates. Template alignment during tape casting is slightly improved by increasing casting speed. There is a correlation between density and texture of the sintered samples. By increasing density, the degree of texture is increased. Maximum achieved texture was F_{111}=42.7% for L3 which had a density of 93.4%. L3 also had the highest direct d_{33}=49$\pm$3 pCN^{-1} and converse d_{33}= 140 pmV^{-1} at 20 kV cm^{-1}.

The further work with this system could take many different paths. Improving the precursor Ti:Ba ratio might prove beneficial if this improves conditions for a topotactic conversion process. Further investigations into improving density should be carried out. A pre-sintering program has reported to improve densities for textured BT [20]. Other alternatives might be to alter sintering temperatures and holding times to optimise density. Although poling was not done the piezoelectric coefficients for the textured BCT show promise and should be investigated further at higher field strengths.

References

1. Jaffe, B., W.R. Cook, and H. Jaffe, *Piezoelectric ceramics*. 1971, London: Academic Press. IX, 317 s. : ill.

2. Rödel, J., W. Jo, K.T.P. Seifert, E.-M. Anton, T. Granzow, and D. Damjanovic, Perspective on the Development of Lead-free Piezoceramics. *Journal of the American Ceramic Society,* 2009. **92**(6): p. 1153-1177.

3. Directive 2002/95/EC of the European Parliament and of the council of 27 January 2003 on the restriction of the use of certain hazardous substances in electrical and electronic equipment. *Official Journal of the European Union,* 2003.

4. Liu, W. and X. Ren, Large Piezoelectric Effect in Pb-Free Ceramics. *Physical Review Letters,* 2009. **103**(25): p. 257602.

5. Kimura, T., *Molten Salt Synthesis of Ceramic Powders*. Advances in Ceramics - Synthesis and Characterization, Processing and Specific Applications. 2011.

6. West, A.R., *Basic solid state chemistry*. 1999: John Wiley & Sons.

7. Troiler-McKinstry, S., *Crystal Chemistry of Piezoelectric Materials*, in *Piezoelectric and Acoustic Materials for Transducer Applications*. 2008, Springer Science + Business Media: Pennsylvania, USA.

8. Haertling, G.H., Ferroelectric Ceramics: History and Technology. *Journal of the American Ceramic Society,* 1999. **82**(4): p. 797-818.

9. Rajagopal, H., P.U.M. Sastry, A. Sequeira, and P. Ramasamy, Single-crystal neutron diffraction study of ferroelectric Ba0·92Ca0·08TiO3. *Bulletin of Materials Science,* 1994. **17**(3): p. 201-204.

10. Tilley, R.J.D., *Crystals and crystal structures*. 2006, Chichester: Wiley. XIII, 255 s. : ill.

11. Moulson, A.J. and J.M. Herbert, *Electroceramics: materials, properties, applications*. 2003, Chichester: Wiley. XIV, 557 s. : ill.

12. Tilley, R.J.D., *Understanding solids: the science of materials*. 2013: Wiley.

13. PhysikInstrumente. Available from: http://www.physikinstrumente.com/tutorial/4_15.html.

14. Kimura, T., Application of texture engineering to piezoelectric ceramics - A review. *Journal of the Ceramic Society of Japan,* 2006. **114**(1325): p. 15-25.

15. Messing, G.L., S. Trolier-McKinstry, E.M. Sabolsky, C. Duran, S. Kwon, B. Brahmaroutu, P. Park, H. Yilmaz, P.W. Rehrig, K.B. Eitel, E. Suvaci, M. Seabaugh, and K.S. Oh, Templated Grain Growth of Textured Piezoelectric Ceramics. *Critical Reviews in Solid State and Materials Sciences,* 2004. **29**(2): p. 45-96.

16. Ohara, Y., K. Koumoto, and H. Yanagida, Barium-Titanate ceramics with high piezoelectricity fabricated from fibrous particles *Journal of the American Ceramic Society,* 1985. **68**(4): p. C108-C109.

17. Poterala, S.F., Y. Chang, T. Clark, R.J. Meyer, and G.L. Messing, Mechanistic Interpretation of the Aurivillius to Perovskite Topochemical Microcrystal Conversion Process. *Chemistry of Materials,* 2010. **22**(6): p. 2061-2068.

18. Rao, C.N.R. and J. Gopalakrishnan, *New directions in solid state chemistry*. 1997, Cambridge: Cambridge University Press. XV, 549 s. : ill.

19. Lotnyk, A., A. Graff, S. Senz, N.D. Zakharov, and D. Hesse, Topotaxial formation of titanium-rich barium titanates during solid state reactions on (110) TiO2 (rutile) and (001) BaTiO3 single crystals. *Solid State Sciences,* 2008. **10**(6): p. 702-708.

20. Sato, T. and T. Kimura, Preparation of <111>-textured BaTiO3 ceramics by templated grain growth method using novel template particles. *Ceramics International,* 2008. **34**(4): p. 757-760.

21. Krasevec, V., M. Drofenik, and D. Kolar, Topotaxy between BaTiO3 and Ba6Ti17O40. *Journal of the American Ceramic Society,* 1987. **70**(8): p. C193-C195.

22. Lv, D., R. Zuo, and S. Su, Processing and Morphology of (111) BaTiO3 Crystal Platelets by a Two-Step Molten Salt Method. *Journal of the American Ceramic Society,* 2012. **95**(6): p. 1838-1842.

23. Lee, S., C.A. Randall, and Z.K. Liu, Modified phase diagram for the barium oxide-titanium dioxide system for the ferroelectric barium titanate. *Journal of the American Ceramic Society,* 2007. **90**(8): p. 2589-2594.

24. Jones, J.L., B.J. Iverson, and K.J. Bowman, Texture and Anisotropy of Polycrystalline Piezoelectrics. *Journal of the American Ceramic Society,* 2007. **90**(8): p. 2297-2314.

25. Kim, H.J., M.J.M. Krane, K.P. Trumble, and K.J. Bowman, Analytical Fluid Flow Models for Tape Casting. *Journal of the American Ceramic Society,* 2006. **89**(9): p. 2769-2775.

26. Davis, M., M. Budimir, D. Damjanovic, and N. Setter, Rotator and extender ferroelectrics: Importance of the shear coefficient to the piezoelectric properties of domain-engineered crystals and ceramics. *Journal of Applied Physics,* 2007. **101**(5).

27. Damjanovic, D., M. Budimir, M. Davis, and N. Setter, Piezoelectric anisotropy: Enhanced piezoelectric response along nonpolar directions in perovskite crystals. *Journal of Materials Science,* 2006. **41**(1): p. 65-76.

28. Mitsui, T. and W.B. Westphal, Dielectric and X-ray studies of CaxBa1-xTiO3 and CaxSr1-xTiO3. *Physical Review,* 1961. **124**(5): p. 1354-&.

29. Lee, H.J., S.O. Ural, L. Chen, K. Uchino, and S. Zhang, High Power Characteristics of Lead-Free Piezoelectric Ceramics. *Journal of the American Ceramic Society,* 2012. **95**(11): p. 3383-3386.

30. Haugen, B.A., *BaCaTiO3 powder analysis*, 2013: Unpublished.

31. Madaro, F., R. Saeterli, J.R. Tolchard, M.-A. Einarsrud, R. Holmestad, and T. Grande, Molten salt synthesis of K4Nb6O17, K2Nb4O11 and KNb3O8 crystals with needle- or plate-like morphology. *CrystEngComm*, 2011. **13**(5): p. 1304-1313.

32. *ISO 5017: Dense shaped refractory product - Determination of bulk density, apparent porosity and true porosity*, 1998, International Organization for Standardization: Switzerland.

33. Kimura, T., Y. Miura, and K. Fuse, Texture development in barium titanate and PMN-PT using hexabarium 17-titanate heterotemplates. *International Journal of Applied Ceramic Technology*, 2005. **2**(1): p. 15-23.

Appendix A - Dilatometer curve of BCT

Dilatometer curve of BCT batch 288 is presented in Figure A.1 [30]. As the temperature is increased the sample starts to contract rapidly at around 1150°C and reaches its maximum density at 1350°C where the contraction stagnates. The appropriate sintering temperature is therefore found at 1350˚C.

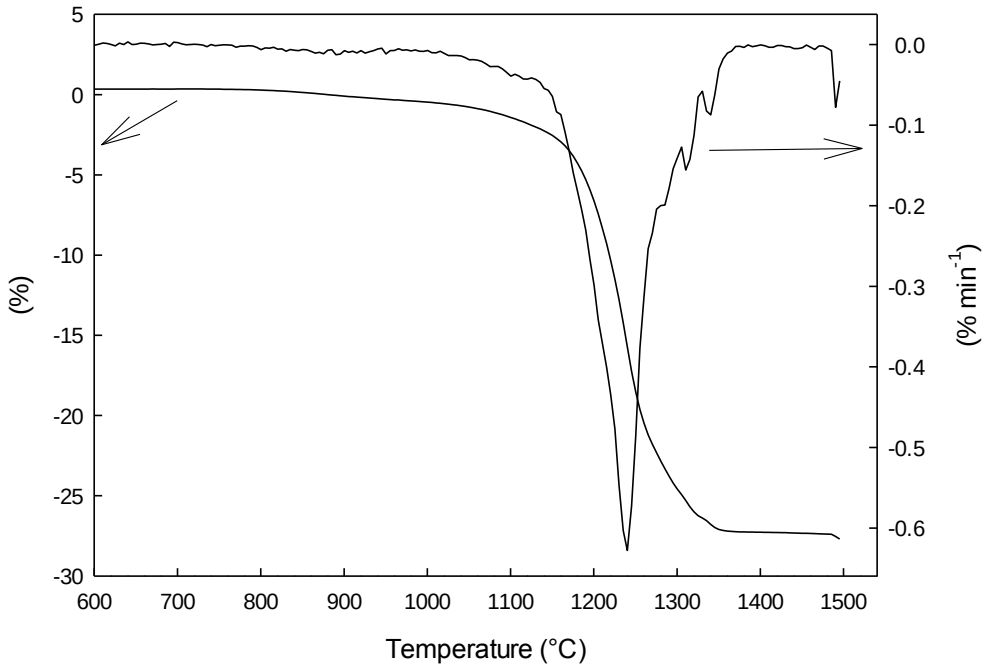

Figure A.1: Dilatometer curve of BCT batch 288, indicating appropriate sintering temperature of 1350˚C.